Microdosimetry of a therapeutic proton beam with a mini-TEPC and a MicroPlus-Bridge detector for RBE assessment

V Conte[1], S Agosteo[2,3], A Bianchi[1,4,5], D Bolst[6], D Bortot[2,3], R Catalano[7], G A P Cirrone[7], P Colautti[1], G Cuttone[7], S Guatelli[6], B James[6], D Mazzucconi[2,3], A B Rosenfeld[6], A Selva[1], L Tran[6] and G Petringa[7]

[1] INFN Laboratori Nazionali di Legnaro, viale dell'Universit`a 2 35020 Legnaro, Italy
[2] Politecnico di Milano, Dipartimento di Energia, via La Masa 34, Milano, Italy
[3] Istituto Nazionale di Fisica Nucleare INFN - Sezione di Milano, via Celoria 16, Milano, Italy
[4] Belgian Nuclear Research Centre, SCK•CEN, Boeretang 200 2400 Mol, Belgium
[5] UHasselt, Faculty of Engineering Technology, Centre for Environmental Sciences, Nuclear Technology Center, Agoralaan 3590 Diepenbeek, Belgium
[6] Centre for Medical Radiation Physics, University of Wollongong, Wollongong NSW 2522, Australia
[7] INFN Laboratori Nazionali del Sud, via S.Sofia 62 95123 Catania, Italy

E-mail: conte@lnl.infn.it

Keywords: microdosimetry, cinical proton beam, RBE assessment, mini-TEPC, MicroPlus Bridge, radiation quality, stocastics of radiation interaction

Abstract

Proton beams are widely used worldwide to treat localized tumours, the lower entrance dose and no exit dose, thus sparing surrounding normal tissues, being the main advantage of this treatment modality compared to conventional photon techniques. Clinical proton beam therapy treatment planning is based on the use of a general relative biological effectiveness (RBE) of 1.1 along the whole beam penetration depth, without taking into account the documented increase in RBE at the end of the depth dose profile, in the Bragg peak and beyond. However, an inaccurate estimation of the RBE can cause both underdose or overdose, in particular it can cause the unfavourable situation of underdosing the tumour and overdosing the normal tissue just beyond the tumour, which limits the treatment success and increases the risk of complications. In view of a more precise dose delivery that takes into account the variation of RBE, experimental microdosimetry offers valuable tools for the quality assurance of LET or RBE-based treatment planning systems. The purpose of this work is to compare the response of two different microdosimetry systems: the mini-TEPC and the MicroPlus-Bridge detector. Microdosimetric spectra were measured across the 62 MeV spread out Bragg peak of CATANA with the mini-TEPC and with the Bridge microdosimeter. The frequency and dose distributions of lineal energy were compared and the different contributions to the spectra were analysed, discussing the effects of different site sizes and chord length distributions. The shape of the lineal energy distributions measured with the two detectors are markedly different, due to the different water-equivalent sizes of the sensitive volumes: 0.85 μm for the TEPC and 17.3 μm for the silicon detector. When the Loncol's biological weighting function is applied to calculate the microdosimetric assessment of the RBE, both detectors lead to results that are consistent with biological survival data for glioma U87 cells. Both the mini-TEPC and the MicroPlus-Bridge detector can be used to assess the RBE variation of a 62 MeV modulated proton beam along its penetration depth. The microdosimetric assessment of the RBE based on the Loncol's weighting function is in good agreement with radiobiological results when the 10% biological uncertainty is taken into account.

1. Introduction

Biological and clinical properties of positively charged particles derive from the physical properties of their interaction with the target volume. When ions penetrate the biological matter, they lose part of their energy,

they slow down and the ionization density along the particle track increases. Because of the increased ionization density, also the amount and complexity of damage to critical cellular structures increases. The relative biological effectiveness (RBE) of ionizing particles is defined as the ratio of the reference radiation dose to the target to the particle radiation dose producing the same biological effect.

RBE depends on several variables, which include radiation type, charge and velocity of the charged particles, dose, fractionation, cell type, biologic endpoint, etc. While for radiotherapy with ions heavier than protons the variability of the RBE is taken into account, a fixed value of 1.1 was and still is the basis for clinical practice with proton beam radiation therapy, as recommended in a joint ICRU-IAEA Report (ICRU Report 78 2007). However, several experiments show that RBE may vary significantly along the proton beam path, especially near the end of the particle range (see for instance Paganetti 2014, Chaudhary *et al* 2014, Guan *et al* 2015, Peeler *et al* 2016, Sørensen *et al* 2017). The RBE variability may mean that the biologically-effective dose distributions received by the patient could differ significantly from what is assumed in the treatment plans and used to define therapeutic prescriptions. This can result in unexpected toxicities and failures to control the tumour (Mohan *et al* 2017, Jones *et al* 2018).

The RBE of different radiation qualities is most frequently represented as a function of the linear energy transfer, LET, both in radiation biology experiments and RBE models, see for instance McNamara *et al* (2015), Ma *et al* (2020). However, the LET is a non-stochastic quantity that describes the mean energy deposition per unit path length, for specified particle type and energy. Several works on analytical LET modelling, some of which were developed for TPS calculations, are available in literature, as a not exhaustive example one can see Marsolat *et al* (2016), Sanchez-Parcerisa *et al* (2016), Hirayama *et al* (2018), Wagenaar *et al* (2020), Deng *et al* (2020), Bertolet *et al* (2020).

Optimized treatment planning that takes into account LET and/or RBE variability would lead to exploit better the potential of proton therapy, reducing the toxicities and the incidence of later-occurring morbidities induced by the radiation treatment (Guan *et al* 2018, Durante 2019).

Currently, different commercial treatment planning software (TPS) for proton therapy are incorporating the capability of calculating LET distributions and RBE prediction based on that in order to perform such optimizations. However, while the dose prescriptions calculated by the TPS are routinely verified with certified ionization chambers as part of the quality assurance (QA) programme in any radiotherapy department, there is no commercial equipment currently available to perform routine verification of LET or RBE distributions calculated by the TPS. It is therefore needed to focus research on this direction. In particular, the devices should be portable, reliable (stable in time) and capable of giving a fast response.

In this context microdosimetry, measuring the random processes of energy deposition in micrometric sites, offers valuable tools to supplement LET or RBE-based treatment planning. In this work the response function in a therapeutic proton beam of a gas miniaturized tissue equivalent proportional counter (mini-TEPC) and of a silicon on insulator (SOI) microdosimeter (MicroPlus-Bridge) are analysed in view of their application for the systematic verification of proton-radiotherapy treatment plans optimized on radiobiology.

2. Material and methods

2.1. The irradiation facility

Microdosimetric measurements were performed at the clinical proton-therapy beam line at the Southern National Laboratories (LNS) of the Italian National Institute for Nuclear Physics (INFN) (Cirrone *et al* 2017) with two different detectors, a gas-based mini-TEPC and a 10 μm thick SOI microdosimeter MicroPlus-Bridge. A limited set of measurements and a partial analysis was already performed in other works (Colautti *et al* 2020, Petringa *et al* 2020) and was extended here to cover the whole SOBP with higher spatial resolution. The SOBP penetration range, measured at R80, the depth corresponding to the 80% of the SOBP distal part dose, was 29.5 mm in water. The depth-dose profile, measured with a Markus plane parallel ion chamber model 23343, is shown in figure 1, together with the measuring positions indicated by crosses (MicroPlus-Bridge detector) and points (mini-TEPC).

A circular collimator, 25 mm in diameter, was placed at the end of the beamline. Figure 2 shows a picture of the mini-TEPC placed in front of the beam collimator, with the main axis of the cylinder perpendicular to the beam direction. A total of 33 and 37 microdosimetric measurements were performed with the mini-TEPC and with the Bridge microdosimetry system respectively, varying the depths by inserting calibrated PMMA layers between the beam collimator and the microdosimeters. A total of 10^6 events were recorded at each measurement position. The PMMA thickness was afterwards converted to water depth using the factor 1.16 derived from the proportionality factor between the depths in water and in PMMA at which the initial 62 MeV protons have reached the same energy, based on SRIM energy-range tables

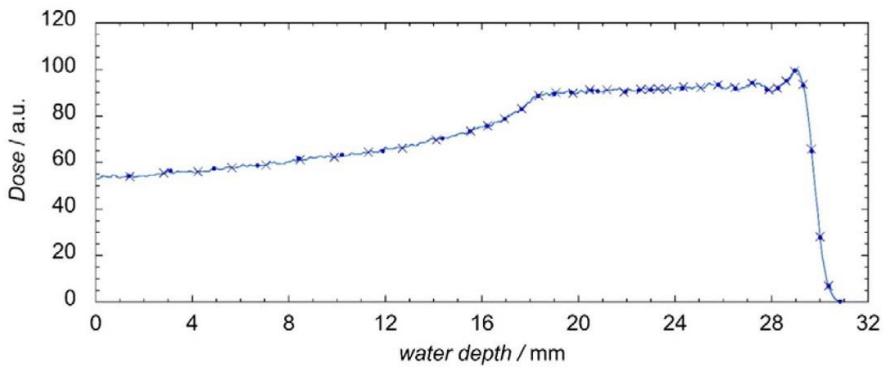


Figure 1. The dose profile of the modulated 62 MeV proton clinical beam. The measurements positions are indicated by crosses (Bridge detector) and points (mini-TEPC).



Figure 2. A picture of the mini-TEPC (left), indicated by the red circle, and the MicroPlus-Bridge microdosimetry system (right) placed in front of the 25 mm beam collimator.

(Ziegler *et al* 2010). Figure 3 shows the depth in water as a function of the depth in PMMA, and the best linear fit to the points.

2.2. Monte Carlo simulations of dose and average LET

The concept of linear energy transfer is widely used to describe the radiation quality. The most general definition of LET for a monoenergetic proton beam is reported in the ICRU60 (ICRU Report 60 1998):

$$\mathrm{LET}_{\Delta} = \frac{\mathrm{d}E_{\Delta}}{\mathrm{d}l} \tag{1}$$

where LET_{Δ} is the electronic stopping power expressed as the ratio between the energy lost by the charged particles due to the electronic collision dE (within a specific Δ value) in a travelled distance dl and the distance dl.

The definition of LET limits its application to only the specified particle type. However, mixed radiation fields, as those generated by non mono-energetic, clinical beams, give rise to a distribution of LET. In these situations, and for practical purposes, an average LET is generally defined to describe the mean value of the stopping powers calculated by averaging the contribution of all particles at a certain point. Most of the energy lost by primary protons in nuclear reactions is, in fact, transferred to secondary charged particles that have short ranges, i.e. one can assume that they are absorbed locally. The averaged LET can serve, therefore, as a good indicator of biological effectiveness (Seltzer 1993, Berger 1993). The two most common implementations of averaged LET are the track-averaged LET ($\overline{\mathrm{LET}}_{\mathrm{t}}$), and the dose-averaged LET ($\overline{\overline{\mathrm{LET}}}_{\mathrm{d}}$) (Wilkens and Oelfke 2002).

Monte Carlo simulations offer a very powerful solution to obtain local energy spectra in a given geometry making use of the information retrieved step-by-step along particles track. Geant4 hence permits a

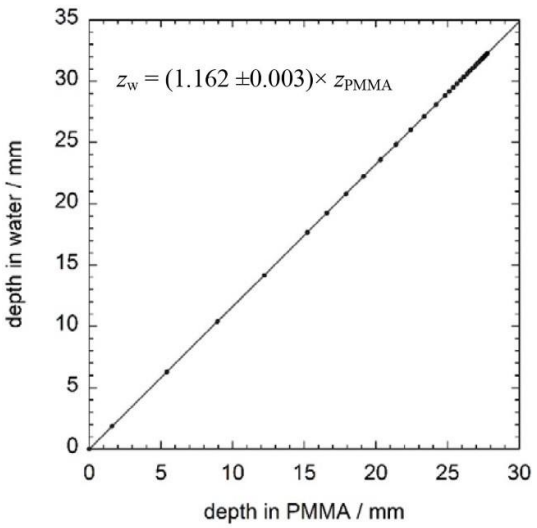


Figure 3. The proton depth in water as a function of the proton depth in PMMA; computed based on the energy-range tables of SRIM.

precise calculation of the ratio between the total energy deposited and the total track lengths from all primary charged particles interacting with a given material, this information being necessary for a precise and reliable estimation of the LET of the radiation in a medium.

The transport beam line of CATANA was simulated with *Hadrontherapy* (Cirrone *et al* 2006), an open source application available in the public release of Geant4 (Allison *et al* 2016). The track-averaged LET ($\overline{\text{LET}}_t$), and the dose-averaged LET ($\overline{\text{LET}}_d$), were calculated with a new module that is described in detail by Petringa *et al* (2020). It uses new algorithms to produce LET results that are independent of the transport parameters such as voxel size, production cut and step length (Petringa *et al* 2017). To calculate $\overline{\text{LET}}_t$ and $\overline{\text{LET}}_d$ at a given water depth *z*, the following equations were used:

$$\overline{\text{LET}}_t(z) = \frac{\sum_{i=1}^{N} L_i l_i}{\sum_{i=1}^{N} l_i} \tag{2}$$

$$\overline{\text{LET}}_d(z) = \frac{\sum_{i=1}^{N} L_i \varepsilon_i}{\sum_{i=1}^{N} \varepsilon_i} \tag{3}$$

where L_i is the electronic stopping power extracted from the Geant4 look-up tables at each particle step *i*, the ε_i and l_i are the energy loss and the particle track length respectively. The scoring technique expressed on equations (2) and (3) for average LET was discussed in other works, especially in what concerns using stopping power look-up tables instead of actual energy loss calculated with Monte Carlo (Cort´es-Giraldo and Carabe 2015, Granville and Sawakuchi 2015, Grassberger *et al* 2011, Giantsoudi *et al* 2013). Following this procedure, it should be noted that the calculated LET is the unrestricted linear energy transfer, LET_∞. When both primary and secondary particles originating from nuclear interactions are considered in the computation, the dose-averaged LET is indicated as total–$\overline{\text{LET}}_d$. When only the contribution of primary protons is considered, the dose-averaged LET is indicated as primary–$\overline{\text{LET}}_d$. Similarly, the primary-$\overline{\text{LET}}_t$ and the total-$\overline{\text{LET}}_t$, which includes the contribution by secondary particles, were also calculated. Within statistical uncertainties, the primary and the total $\overline{\text{LET}}_t$ were found to be the same.

2.3. Microdosimetric distributions and average quantities

As already mentioned in the introduction, the key to understand the radiation effects lies in the spatial distribution of the energy deposition events at cellular and subcellular level, and in the complexity of damages that this can cause, rather than in LET that is only an approximate descriptor of particle track structure.

Microdosimetry detectors measure the pulse height distribution of signals produced by the passage of each single particle within the sensitive volume (SV) or in its surrounding (via delta electrons). The amplitude of the pulse is proportional to the original number of ionizations produced per single event, and in turn to the energy imparted from a single event ε_1, assuming that a constant W-value can be applied to the whole spectrum of particles and charge collection in SV is 100%. The fundamental microdosimetric quantity

is the *lineal energy*, y, defined as the ratio of ε_1 to the mean chord length of the target volume and expressed in units of keV/μm. Being a stochastic quantity, y is characterized by a probability density $f(y)$. The dose probability density $d(y)$ is also considered, which is related to *f(y)* through the following equation:

$$d(y) = \frac{yf(y)}{\int_0^\infty yf(y)\,dy}. \tag{4}$$

The frequency mean lineal energy, $\bar{y}_F$, and the dose mean lineal energy, $\bar{y}_D$, can be computed as the first moments of the distributions $f(y)$ and $d(y)$ respectively:

$$\bar{y}_F = \int_0^\infty yf(y)\,dy; \quad \bar{y}_D = \int_0^\infty yd(y)\,dy. \tag{5}$$

A detail discussion on microdosimetric quantities is given in (ICRU Report 36 1983). It should be observed that $\bar{y}_D$ is the ratio of the second to the first moments of the $f(y)$ distribution:

$$\bar{y}_D = \frac{\int_0^\infty y^2 f(y)\,dy}{\int_0^\infty yf(y)\,dy} = \frac{m_2}{m_1}. \tag{6}$$

The relative variance of the distribution can be expressed in terms of $\bar{y}_F$ and $\bar{y}_D$ (Kellerer 1985):

$$\frac{\mathrm{Var}(y)}{(\bar{y}_F)^2} = \frac{\bar{y}_D}{\bar{y}_F} - 1. \tag{7}$$

Lineal energy is by definition a stochastic quantity; it is dimensionally equivalent to LET, which is however an average property that neglects the random nature of energy loss along a track and it is not measurable. The stochastic processes leading to the formation of the lineal energy y include several random variables, the distribution of LET of all interacting particles, the energy straggling, the variability of path lengths, the gas gain distribution, the delta ray contribution, etc. Therefore, in general, the relative variance of the lineal energy distribution is larger than the relative variance of the distribution of LET for interacting particles, and $\bar{y}_D > \overline{\mathrm{LET}}_d$, being $\overline{\mathrm{LET}}_d$ the dose-averaged LET. However, when the primary particle velocity is high a significant fraction of secondary electrons escapes the target volume, depositing part of their energy out of it. In this case the mean lineal energy can be lower than unrestricted LET and rather corresponds to restricted LET.

2.4. The mini-TEPC: detector, data acquisition and lineal energy calibration

The mini-TEPC used for this measurement campaign is an upgraded version of the miniaturized TEPC developed at the Legnaro National Laboratories of the Italian National institute for Nuclear Physics (INFN-LNL) and described in (De Nardo *et al* 2004). The only modification with respect to the previous model is an enlargement of the gas ducts to facilitate the counter cleaning procedures, the rest of the design has remained the same. The cylindrical SV has both diameter and height of 0.9 mm, the cathode is made of a 0.35 mm-thick A-150 wall, surrounded by a 0.35 mm-thick Rexolite® insulator and a 0.2 mm-thick titanium sleeve for a total external diameter of 2.7 mm. The anode is a 10 μm gold plated tungsten wire. The water-equivalent wall thickness of the detector is 1.37 mm, as it results by considering the average stopping-power ratio of protons within the different materials. Figure 4 shows a drawing of the detector. This new mini-TEPC operates in gas-steady modality, without gas flow. The detector was filled with pure propane at a gas pressure of 45.4 kPa, corresponding to a SV mass thickness of 0.075 mg cm^{-2} of gaseous propane. Multiplied by the mean ratio of mass-stopping powers of protons in propane and water, calculated with SRIM (Ziegler *et al* 2010), and by the water unit density, the equivalent site size in water is 0.85 μm.

Signals from the counter anode are fed into a customized low noise charge-sensitive preamplifier with a dynamic range of more than four orders of magnitude. The output of the preamplifier is then sent to two linear pulse-shaping amplifiers operated in parallel, with gain settings in the ratio 10:1. The Gaussian-shaped pulses are then digitized by a 14-bit ORTEC Model AD114 and a 13-bit ORTEC Model AD413 CAMAC-ADCs. The two sub-spectra are joint offline by matching the overlapping event-size regions.

A shaping time of 0.5 μs was chosen during these measurements as the best compromise between low noise and counting rate capabilities.

In all measurements, the beam current has been adjusted to get a constant counting rate of 10^4 counts per second.

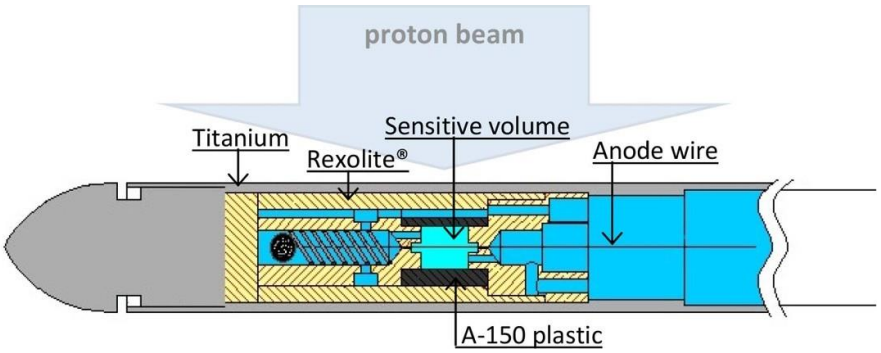


Figure 4. A drawing of the mini-TEPC.

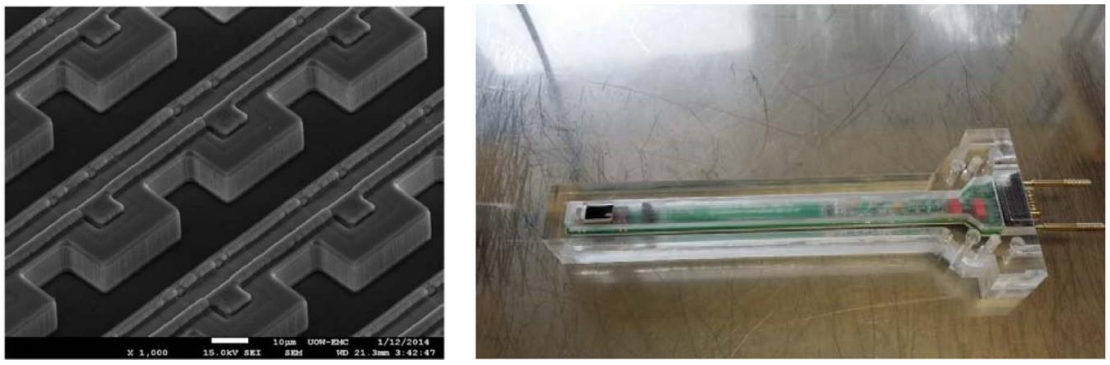


Figure 5. Left: Bridge microdosimeter: fragment of array of 3D SVs with dimension 30 × 30 × 10 μm^3 each; right: a waterproof PMMA sheath containing the Bridge microdosimeter connected to the MicroPlus probe, which provides a low noise readout with a DIL20 chip package.

The lineal energy calibration of spectra was performed by using the proton-edge technique (Waker 1985, Conte *et al* 2013). The value of 143 keV μm^{-1} was assigned to the flex position of the Fermi-like function fitted to the p-edge region, as described in (Conte *et al* 2019).

In terms of lineal energy, the low threshold value of the measured spectra resulted to be approximately 0.3 keV μm^{-1}. As usual, experimental *f(y)* data points were then fitted with a linear function in the *y* region between 0.3 keV μm^{-1} and 0.4 keV μm^{-1} and extrapolated down to 0.01 keV μm^{-1}.

2.5. The MicroPlus-Bridge: detector, data acquisition and lineal energy calibration

The silicon detector used in this study is the Bridge Microdosimeter, designed by the Centre for Medical Radiation Physics (CMRP), University of Wollongong, Australia. The Bridge microdosimeter consists of an array of 3D right parallelepiped (RPP) shape SVs with area 30 μm × 30 μm each, constructed on a silicon-on-insulator (SOI) wafer with an active silicon thickness of 10 μm. Figure 5 shows a SEM image of a fragment of the Bridge microdosimeter (left) and the final assembling of the MicroPlus-Bridge microdosimeter (right). The microdosimeter is connected to an in-house designed low noise optimized preamplifier and shaping amplifier, enabling the detection of lineal energies as low as ~0.2 keV μm^{-1} in silicon. Additional details on the MicroPlus-Bridge microdosimeter technology can be found elsewhere (Rosenfeld 2016).

Pulse height spectra for the incident protons was measured using an ORTEC Easy-MCA multichannel analyser connected to a portable computer. The detector was biased with 9.5 V. Energy calibration was performed using a calibrated pulse generator to convert the channel number to energy imparted ε_1. In turn, the pulse generator was calibrated with a 300 μm thick planar, silicon, fully depleted Hamamatsu diode, of capacitance similar to that of the Bridge detector (Tran *et al* 2015, Anderson *et al* 2017), using the charge collection corresponding to the energy deposited by alpha particles from a sealed ^{244}Cm source, with 5.18 MeV in mean energy or from ^{148}Gd with alpha particle energy equal to 3.183 MeV and a range in silicon of about 10 μm. The calibration of the Bridge detector is facilitated by its linear response. The mean path length of protons crossing the active silicon layer is almost equal to the silicon thickness and differs from the mean chord length for randomly oriented tracks. As recommended in a previous work (Bolst *et al* 2017), the

lineal energy was calculated by dividing the energy imparted ε_1 by the mean path length rather than by the mean chord length. The water equivalent mean path length, that is the water equivalent thickness corresponding to the 10 μm silicon thickness, is 17.3 μm for irradiation with a parallel proton beam (Guatelli *et al* 2008).

In terms of lineal energy *y*, for these measurements the minimum detectable signal above the noise level was approximately 0.5 keV μm^{-1} (tissue). As was done for the mini-TEPC, *f(y)* event-size distributions were fitted with a linear function in the *y* region between 0.5 keV μm^{-1} and 0.6 keV μm^{-1} and extrapolated down to 0.01 keV μm^{-1}.

2.6. Data analysis

The frequency and dose distributions of the lineal energy measured at the same positions with the mini-TEPC and the MicroPlus-Bridge microdosimeter were compared and the spectral differences were discussed in order to analyse the different stochastics of energy deposition in the different SV. As described in the previous sections, the water-equivalent size of the mini-TEPC is 0.85 μm while that of the MicroPlus-Bridge microdosimeter is 17.3 μm; in addition, the SVs have different shape, therefore also different chord length distributions. Consequently, it is expected that the stochastic distributions of the lineal energy measured with the two detectors are different, in particular close to the end of the proton range, where protons with energy less than about 720 keV traverse completely the mini-TEPC SV but stop inside the silicon thickness. The aim of the comparison was to discuss the differences, analysing the physical processes leading to the different spectral contributions.

Because of their closer correlation with the biological impact of irradiation, dose distributions *y*d(*y*) are generally reported rather than the frequency distributions *yf(y)*, while the horizontal axis is in a log scale. However, a closer view to both distributions can be useful to understand the different contributions to the spectra formation.

The statistical uncertainty on the lineal energy distributions was calculated by taking the square root of the number of measured events in each lineal energy bin.

The frequency and the dose mean values of the lineal energy, $\bar{y}_F$ and $\bar{y}_D$, were also calculated and compared with calculated mean values of unrestricted LET, in view of a possible use of the microdosimeters for the QA of LET-based treatment planning systems. The lineal energy calibration procedure resulted in a 'type A' standard uncertainty smaller than 5%, as evaluated by repeated measurements at a specific position. Systematic uncertainties related to the stopping power tables were not considered in this work. The uncertainties on $\bar{y}_F$ and $\bar{y}_D$ were determined by error propagation following the uncertainty in the number of counts and that on the lineal energy calibration.

Finally, the capability of the two microdosimeters to describe the RBE variation along the proton penetration depth was investigated. An estimation of RBE can be performed, starting from the experimental microdosimetric dose distributions d(*y*) and using the Loncol's biological weighting function r(*y*) (Loncol *et al* 1994), according to the following equation:

$$RBE_{micro}(z) = \int_{0.01}^{\hat{y}_{max}} r(y)\ d(y, z)\, dy \tag{8}$$

where *z* is the water depth and d(*y*, *z*) is the microdosimetric dose distribution measured at depth *z*. The shape of the Loncol's biological weighting function r(*y*) is shown in figure 6.

Equation (8) was applied to the experimental dose distributions d(*y*) measured with the mini-TEPC and the MicroPlus-Bridge microdosimeter to derive the corresponding RBE_{micro} values. These values were afterwards scaled by a constant factor in order to get the reference value RBE = 1.1 at the entrance point:

$$RBE_{micro}(z) = \frac{RBE_{micro}(z)}{RBE_{micro}(z = 1.4\ mm)} \cdot 1.1. \tag{9}$$

The use of the Loncol's biological weighting function *r(y)*, and the normalization of the results through equation (9), rest on previous experimental evidence that, despite the function *r(y)* was derived for a specific biological end-point (early intestinal intolerance assessed by crypt regeneration in mice in vivo), it can reproduce the RBE_{10} variation as a function of depth for different cell lines, therefore for *in vitro* RBE (De Nardo *et al* 2004). The uncertainty in the $RBE_{micro,scaled}(z)$ is dominated by the uncertainty in the Loncol weighting function, which was however not considered. Instead, the uncertainties in the number of counts in each energy bin of the d(*y*) distributions were propagated.

Previous works report the RBE assessment via microdosimetry based on application of the microdosimetric kinetic model (MKM) (Bianchi *et al* 2020, Debrot *et al* 2018). Though, one distinction

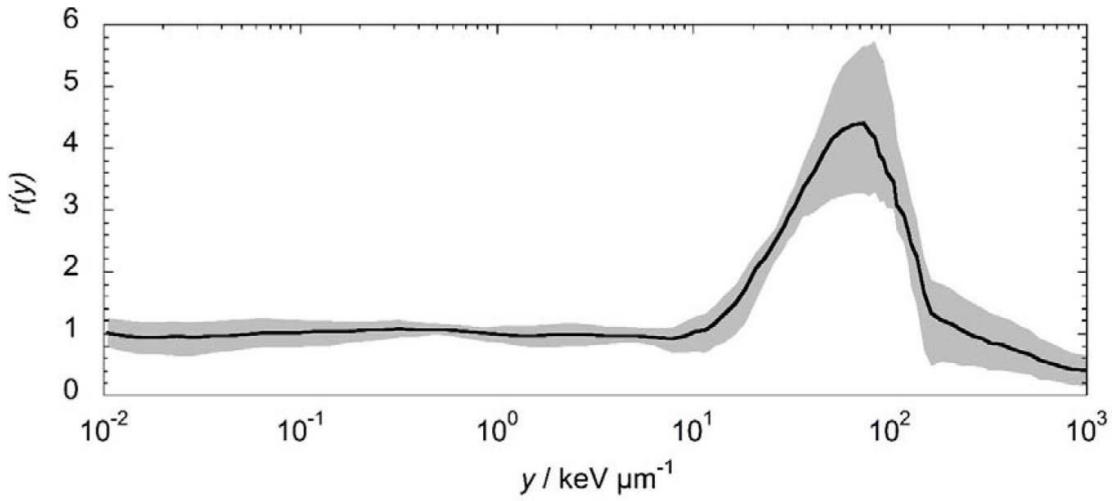


Figure 6. The Loncol's biological weighting function **r*(y)*** (Loncol *et al* 1994). The grey area represents the region within ±1 standard deviation.

between the MKM and Loncol's method, is that the use of a weighting function allows to consider each value of the microscopic dose distribution of the lineal energy d*(y)* and not only the average values $\bar{y}_D$ or y^*. Since different distributions d*(y)* can have the same $\bar{y}_D$ or y^*, the Loncol's method is more sensitive to differences in the radiation field than the MKM, therefore this approach was preferred in this work.

3. Results and discussion

3.1. Microdosimetric spectra

The two sets of microdosimetric dose distributions measured with the mini-TEPC and with the MicroPlus-Bridge system are shown in figures 7 and 8, respectively. Distributions are presented as *y*d*(y)* versus *y* on a logarithmic abscissa to facilitate visual interpretation. In this representation, the area under the curve between two values of *y* is proportional to the fraction of physical absorbed dose due to the events in that interval. For further details on the meaning of the area under the curve with logscale *x*-axis the reader can refers to ICRU36, appendix B (ICRU Report 36 1983). In both figures 7 and 8 the leftmost blue curve corresponds to the entrance position, while the rightmost red curve corresponds to the last position beyond the Bragg peak. It is clearly visible that the distributions move towards higher *y*-values for increasing penetration depth, reflecting the increasing of LET as the protons slow down. In figure 8 a sharp end at about 40 keV µm^{-1} is quite noticeable, which will be discussed later in section 3.3.

A difference in the two figures immediately catches the eye, data from the mini-TEPC show much broader distributions and overall, the spectra span over a wider range of lineal energy *y*, starting from about 0.1 keV µm^{-1} and extending beyond 100 keV µm^{-1}. On the other hand, the spectra measured by the MicroPlus-Bridge detector are always narrower and span over a limited range of *y*, with minimum event size at about 0.4 keV µm^{-1} and maximum event size slightly above 40 keV µm^{-1}. In both figures, there are also a few large size events, up to about 700 keV µm^{-1} for the mini-TEPC and about 100 keV µm^{-1} for the Bridge detector, likely caused by the high-LET fragments of the target nuclei produced by primary protons in nuclear interactions. A much broader distribution of microdosimetric spectra especially in the entrance region is determined mostly by a much larger energy straggling in 0.85 µm SV of the mini-TEPC in comparison to the 17.3 µm SV of the Bridge microdosimeter. It also leads to a $\bar{y}_D$ measured by TEPC that is higher than the one measured by Bridge in the entrance region (to be discussed later). This interpretation is consistent with other experimental results (Bianchi *et al* 2020) and with Monte Carlo Geant4 simulations (Bolst *et al* 2020), showing that the distributions for silicon microdosimeters and for mini-TEPC are similar when the SVs have approximately the same size.

3.2. Frequency and dose lineal energy distributions

Figure 9 shows both the frequency and the dose lineal energy distributions measured with the mini-TEPC (left panel) and with the Bridge microdosimeter (right panel) at the smallest depth z = 1.4 mm and beyond the Bragg peak, at depth z = 30.4 mm. The log-linear plot for the frequency distribution has the same meaning as before: the area under the curve *y*f*(y)* over a given interval of *y*-values is proportional to the

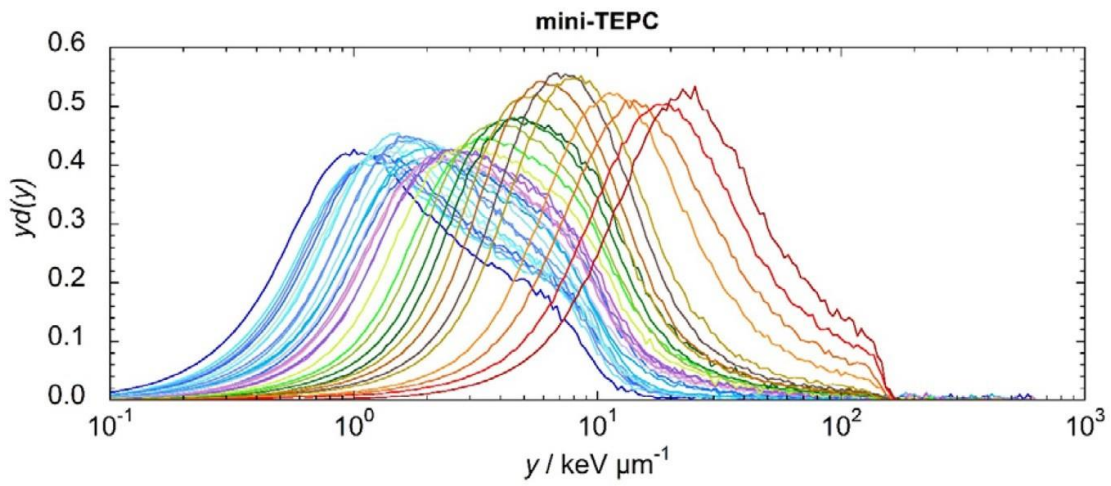


Figure 7. Microdosimetric spectra measured with the mini-TEPC at 33 positions across the proton SOBP, as shown in figure 1. The leftmost blue line corresponds to the first position at water-equivalent depth z = 1.4 mm, the rightmost red line corresponds to the last position at depth z = 30.8 mm.

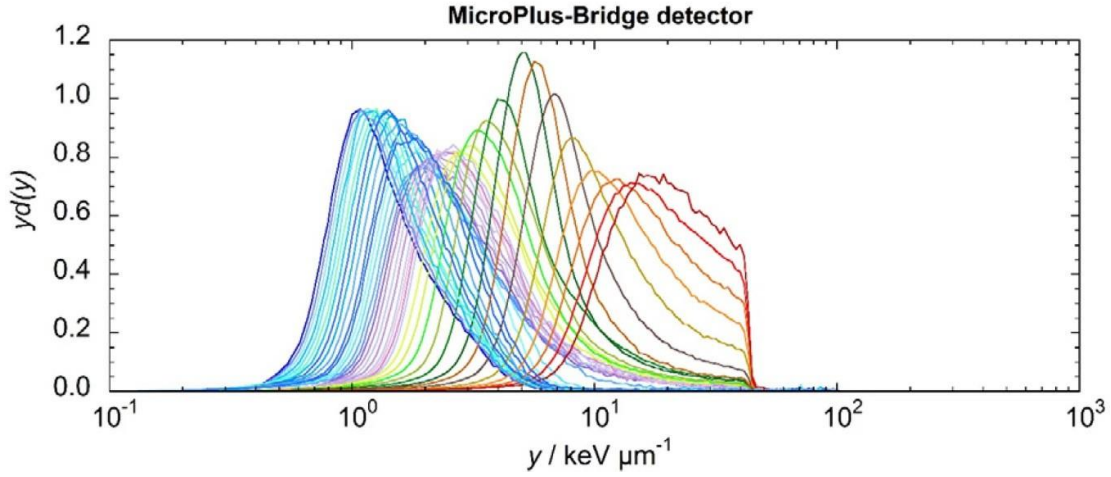


Figure 8. Microdosimetric spectra measured with the MicroPlus-Bridge detector at 37 positions across the proton SOBP, as shown in figure 1. The leftmost blue line corresponds to the first position at water-equivalent depth z = 1.4 mm, the rightmost red line corresponds to the last position at depth z = 30.4 mm.

fraction of events in that y-interval. The position on the y-axis of the thin and the thick short vertical lines indicate the values of the frequency and the dose mean lineal energy, $\bar{y}_F$ and $\bar{y}_D$, respectively, calculated as the first moments of the distributions $f(y)$ and $d(y)$.

At the entrance position (top panels), the frequency lineal energy distribution $yf(y)$ from the mini-TEPC is much broader than that of the MicroPlus-Bridge detector and it shows a higher contribution of small size events. It should be mentioned that the measured distributions of energy deposit are due to various stochastic factors among which the LET distribution of the radiation field (equal for both detectors) is only one. In particular, the energy deposited per event in the gaseous cavity of the mini-TEPC (0.85 µm simulated site–size) is smaller than that deposited in the silicon active layer (17.3 µm simulated site–size), hence the relative variance due to energy straggling is larger for the mini-TEPC. The chord length variability is also larger for the gas detector, due to its cylindrical shape, further contributing to enlarge the distribution of energy deposition. The gas avalanche stochastics of the mini-TEPC also increases the variance of the measured event-size distribution, though this factor seems to contribute only to a minor extent: indeed, experiments and Monte Carlo FLUKA simulations, which do not take into account the gas avalanche, generally show a good agreement (Rollet *et al* 2010, 2011, Mazzucconi *et al* 2019). At depth z = 30.4 mm (bottom panels), the fraction of small event sizes to the left of the main peak in the $yf(y)$ spectra is due to electrons, either delta-rays produced by protons that pass outside the site or Compton electrons by prompt gamma rays produced in the TEPC wall or in the PMMA layers (Polf *et al* 2014). Though visible in the

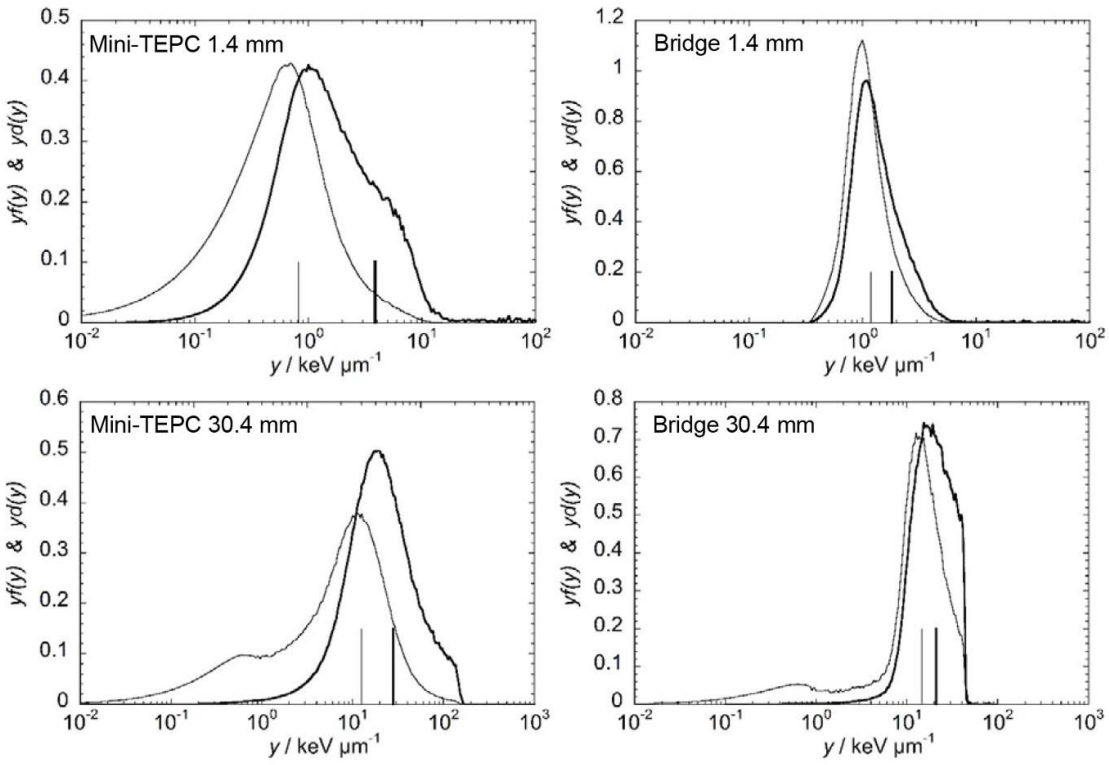


Figure 9. Frequency and dose-weighted lineal energy distributions measured with the mini-TEPC (left) and with the MicroPlus-Bridge microdosimeter (right) at water-equivalent depth z = 1.4 mm (top) and z = 30.4 mm (bottom). The short vertical lines indicate in the horizontal axis the frequency (thin line) and dose (thick line) mean lineal energy values, $\bar{y}_F$ and $\bar{y}_D$, respectively.

frequency distributions, these small events give a negligible contribution to the *yd(y)* spectra. That because weighting the f*(y)* distribution with *y* depresses the partial contribution of small *y* and increases that of greater size. The difference between the dose and frequency mean lineal energies $\bar{y}_D$ and $\bar{y}_F$ is maximum at the entrance and decreases when approaching the Bragg peak.

3.3. Spectral differences in the y*d*(y) distributions

In order to analyse the differences in the *yd(y)* distributions of the two detectors more in detail, figure 10 shows pairwise measurements performed at six specific significant depths, also indicated in the figures as black dots in the depth-dose curve. Short vertical lines represent the frequency and dose-mean lineal energy values calculated from the two distributions.

What was already observed in figure 9, is also confirmed for the other positions along the SOBP: at all depths, the distribution measured by the mini-TEPC is broader than the corresponding one measured by the MicroPlus-Bridge microdosimetry system, mostly as an effect of the larger energy straggling in the smaller SV volume of the mini-TEPC.

As observed in figure 9, at the left side of the peak the distributions measured with the mini-TEPC increase more slowly, revealing a larger fraction of small *y* events, already discussed in the previous paragraph. The spectra measured with the mini-TEPC in the proximal region (top panels) show a smooth shoulder between 5 keV µm^{-1} and 15 keV µm^{-1}. Moving deeper this shoulder is absorbed inside the main peak. A similar shoulder is not observable in the MicroPlus-Bridge spectra. These events are likely due to electrons produced mainly in the detector walls: Compton electrons by x-rays and delta-electrons from indirect events, i.e. protons passing outside the SV and interacting with it only through the injected secondary electrons. As discussed elsewhere (Conte *et al* 2013) the electron edge (corresponding to the maximum energy which electrons can deposit in the SV) in 1 µm site-size is about y_{e-edge} = 10 keV μm^{-1}, which is consistent with the position of the observed shoulder. Considering practical range expressions (Weber *et al* 1964; Kobetich and Katz 1969), the maximum energy deposition by electrons in the silicon detector (about 40 µm of maximum chord length for isotropic irradiation) is about 80 keV. Dividing 80 keV by the water equivalent chord length of 17.3 µm, an electron edge at about y_{e-edge} = 4.5 keV μm^{-1} can be evaluated, therefore in the silicon device electrons and protons events have similar size at the entrance. In the

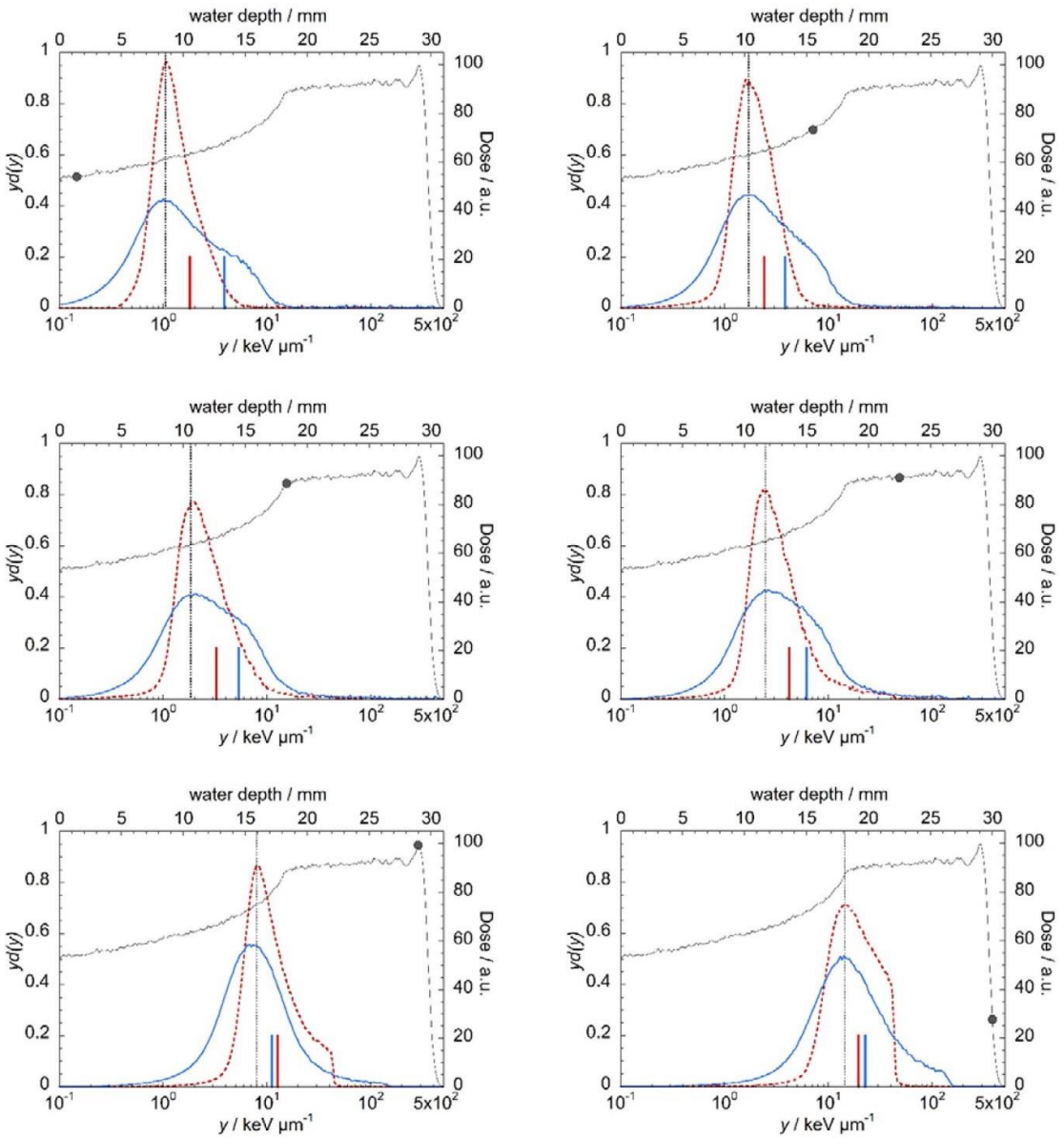


Figure 10. Pairwise microdosimetric *yd(y)* spectra measured with the two different detectors at specific depths, indicated as black dots in the depth dose profile. Blue line: mini-TEPC; red dashed line: MicroPlus-Bridge detector. The vertical black dot line identifies the position of the peak in the Bridge spectrum. Vertical short lines indicate the value of the dose-mean lineal energy for the mini-TEPC (blue line) and for the Bridge detector (red line).

mini-TEPC these Compton and delta electrons are generated mostly in the cavity wall while in the Bridge they are coming from the PMMA layer in front of it.

Approaching the Bragg peak and beyond it, a definite fall-off appears in the distribution of both detectors, corresponding to the proton edge (p-edge), being more evident and sharper for the silicon device. The p-edge is produced by the maximum energy that protons can deposit in the SV. For micrometric dimensions, the maximum energy deposited is approximately the product of the maximum stopping power by the maximum chord length, assuming that the range of these protons is larger than average chord of the equivalent SV (0.85 µm in case of Mini-TEPC). In turn, the lineal energy at the p-edge is the quotient of the maximum energy deposit and the mean chord length. For the mini-TEPC the position of the proton edge corresponds approximately to the maximum stopping power of protons, since protons at maximum stopping powers release the maximum amount of energy in less than 1 µm depth. Instead, in the silicon device protons at the maximum stopping power stop inside the 10 µm detector thickness depositing all their energy in the SV. Protons of higher energy and smaller stopping power with projected range ≤10 µm also deposit all their energy in the SV; therefore, the energy deposit is maximum for those protons that stop exactly at the exit surface of the SV. These protons have energy of 721 keV according to NIST (PSTAR) and 716 keV according to SRIM. Considering the equivalent water-thickness of 17.3 µm, the corresponding p-edge lineal

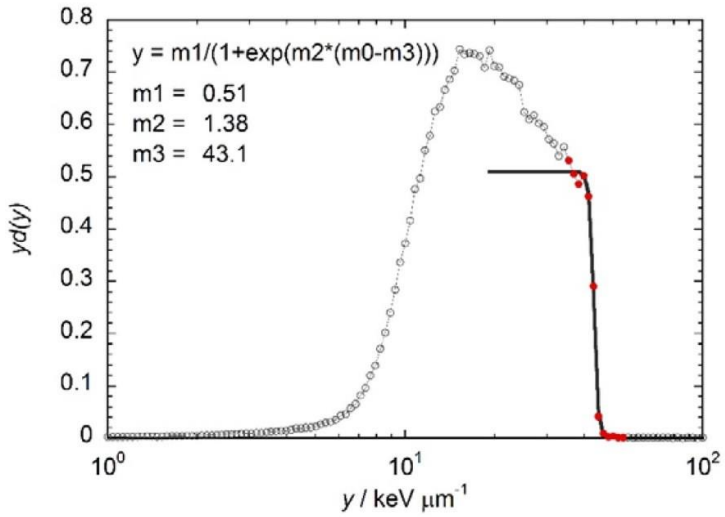


Figure 11. The proton-edge region measured by the MicroPlus-Bridge system and fitted by a Fermi-like function (thick line). The Fermi-like function has been extrapolated beyond the domain of the fitted points.

energy values are 41.8 keV µm^{-1} and 41.5 keV µm^{-1} respectively. Figure 11 shows the best fitting with a Fermi-like function of the p-edge region in the Bridge microdosimetric spectrum measured at a water depth z = 30.4 mm. The position of the flex is at y = 43.1 keV µm^{-1}, which is in good agreement with the maximum lineal energy of protons in 10 µm of silicon, evaluated according to NIST (PSTAR) and SRIM energy range tables. This finding can be interpreted as a crosscheck of two independent calibration techniques, using an alpha source and the p-edge for the Bridge detector and the mini-TEPC, respectively. The two procedures lead to results that are consistent with each other.

Considering the Bridge spectra, protons with energy lower than 721 keV stop and deposit all of their energy inside the detector, increasing the dose contribution in the *y*-region just below the *p*-edge. On the other hand, considering the mini-TEPC, 721 keV protons pass through the gas cavity without stopping in it, and have a stopping power in water of 29.3 keV µm^{-1} (SRIM), which corresponds to a lineal energy of about 37.3 keV µm^{-1}. Protons remain crossers down to an energy of about 75 keV, therefore events due to protons of energy between 76 keV and 721 keV, which for the MicroPlus-Bridge detector accumulate below 42 keV µm^{-1}, in the case of the mini TEPC are distributed up to 143 keV µm^{-1}. This means that in the last 17–20 microns of the proton range (distal part) most events will be stoppers in SOI Bridge, hence they do not contribute to the high LET portion of the microdosimetric spectra.

The *yd(y)* distributions show a peak, which is sharper for the Bridge detector, as a result of the larger SV (Bolst *et al* 2020). At any depth, the position of the peak in the *yd(y)* spectra is about the same for both detectors, as indicated by the dotted line in figure 10, and corresponds approximately to LET of the most probable particles at the specific depth. For instance, in the first measuring position the peak is at about $y \approx 1.1$ keV µm^{-1}, which corresponds to the stopping power of 62 MeV protons in water, S_{water} = 1.065 keV µm^{-1}, according to SRIM calculations.

3.4. Contribution by large size events to the microdosimetric spectra

In addition to what has been discussed in the previous paragraphs, a close view to figure 10, in particular to the top panels, reveals the presence of some rare events at high *y* values. These rare events are likely energy depositions by high LET fragments produced in nuclear interactions of protons with the target nuclei. For the mini-TEPC the detected fragments are produced mainly in the A150 plastic, those detected by the MicroPlus-Bridge counter are produced by fragmentation of carbon and oxygen ions in the PMMA layer in front of the detector. To better visualize these rare events, the *yd(y)* distributions measured with the two detectors at a depth z = 1.4 mm are plotted in figure 12 (left panel) in a log-log scale. It can be observed that the maximum size of the events detected by the mini-TEPC is about 640 keV µm^{-1}, which corresponds to an energy deposit of about 430 keV in the gas cavity. The maximum size of events detected by the Bridge microdosimeter is about 100 keV µm^{-1}, corresponding to an energy deposit of 1.7 MeV in the silicon active layer. This difference is consistent with the contribution of target fragments that have high LET and very short range, so that they stop completely inside the silicon thickness but still can cross the mini-TEPC cavity. The relative frequency of these events beyond the large peaks is low: the fraction of events in the mini-TEPC with $y > 20$ keV µm^{-1} is $1.5 \cdot 10^{-4}$, while the correspondent dose fraction is $1.2 \cdot 10^{-2}$; for the

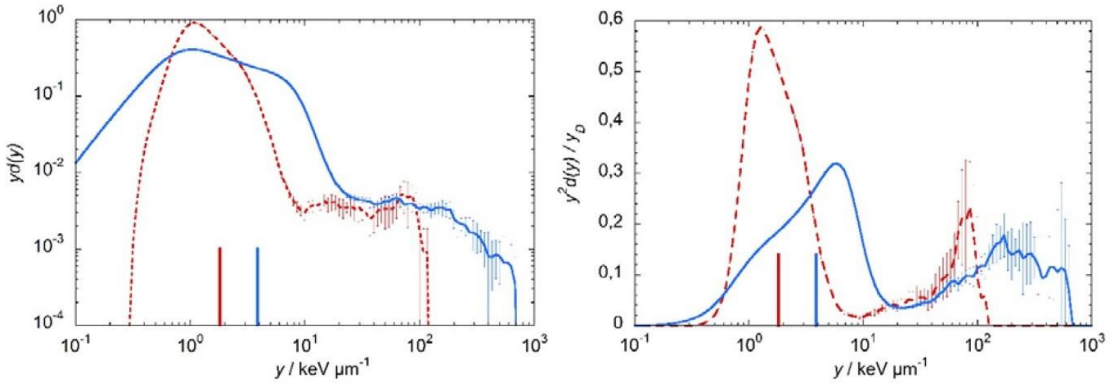


Figure 12. Pairwise spectra measured with the mini-TEPC (blue line) and the MicroPlus-Bridge detector (dashed red line) at depth z = 1.4 mm. Lineal energy spectra binned at 30 points per decade. Vertical error bars represent the statistical uncertainties on the number of counts in each lineal energy bin. Vertical short lines indicate the value of the mean lineal energy for the mini-TEPC (blue) and for the Bridge detector (red). More details in the text.

MicroPlus-Bridge detector the fraction of events with $y > 10$ keV µm^{-1} is $4 \cdot 10^{-4}$ and the correspondent dose fraction is $0.9 \cdot 10^{-2}$. The contribution of these rare events to the total dose is therefore of the order of 1%; however, the effect on the dose-mean lineal energy value is higher: when considering an upper limit of 20 keV µm^{-1} for its calculation, the $\bar{y}_D$ measured by the mini-TEPC decreases from $\bar{y}_D$ = 3.87 keV µm^{-1} to $\bar{y}_{D,20}$ = 2.14 keV µm^{-1}. By setting the upper limit in the Bridge spectrum at 10 keV µm^{-1} the mean lineal energy decreases from $\bar{y}_D$ = 1.81 keV µm^{-1} to $\bar{y}_{D,10}$ = 1.46 keV µm^{-1}. To visualize the contribution of different y-intervals to the total $\bar{y}_D$, the right panel of figure 12 shows the distribution $y^2 d(y)/\bar{y}_D$ versus y in a logarithmic abscissa. In a similar way as for the representation of figure 6, the area under the curve between two values of y is proportional to the fraction of $\bar{y}_D$ ascribable to the events in that interval. It can be easily recognised by eye that the contribution of fragments to $\bar{y}_D$ is equal to almost 50% for the mini-TEPC and to about 20% for the MicroPlus-Bridge detector.

In order to analyse the contribution of these high-y events at different penetration depths, figure 13 shows the microdosimetric spectra measured with the mini-TEPC (middle panel) and with the Bridge detector (bottom panel) at five relevant positions across the SOBP, indicated by coloured arrows in the depth-dose profile shown in the top panel of the same figure. In the top panel the computed primary and the total dose-averaged $\overline{\text{LET}}_d$ are also shown for further discussion. The microdosimetric spectra are shown as $y^2 d(y)/\bar{y}_D$ distributions: as already mentioned, equal areas under the curves represent equal contributions to $\bar{y}_D$ due to events in the corresponding y-interval. The impact of the high size events on $\bar{y}_D$ is maximum in the first two measuring positions, upstream of SOBP plateau, then it decreases moving forward (mid-SOBP) and almost disappears in proximity of the Bragg peak (last two positions). This trend is very similar for the mini-TEPC and the MicroPlus-Bridge detector and is consistent with results of Monte Carlo simulations for the primary and total dose-averaged LET. The effect of the secondary charged particles from nuclear reactions is almost negligible in the region where the $\overline{\text{LET}}_d$ increases rapidly, beyond z = 28 mm, while it is considerable in the entrance region, up to the SOBP plateau. These results are consistent with recent studies (Paganetti *et al* 2002, Tommasino and Durante 2015) demonstrating that secondary target fragments contribute to the overall dose deposited in the patient especially in the entrance channel giving a non-negligible dose to healthy tissues surrounding the tumour, thus potentially increasing secondary cancer risks induced by proton therapy.

3.5. Comparison of mean lineal energy values

Mean lineal energy values were derived from microdosimetric spectra using equation (5). The summary of all results obtained at the different positions is given in table1. Figure 14 shows the frequency mean lineal energy, $\bar{y}_F$, as a function of depth together with the track-averaged LET, $\overline{\text{LET}}_t$, calculated with equation (1). The values obtained with the MicroPlus-Bridge detector are consistent with calculated $\overline{\text{LET}}_t$ values, within ±5% uncertainty on $\bar{y}_F(z)$ and ±0.3 mm uncertainty on the depth position. The values derived from the mini-TEPC distributions are always lower than those derived from the MicroPlus-Bridge detector, and also lower than the simulated $\overline{\text{LET}}_t$, the difference being approximately a constant factor 1.5 (Conte *et al* 2019); when this factor is applied the values of the mini-TEPC are in good agreement with $\overline{\text{LET}}_t$ and those obtained with the MicroPlus-Bridge detector as shown in the bottom panel of figure 14. Hence, the $\bar{y}_F(z)$ measured with the mini-TEPC is proportional to the simulated $\overline{\text{LET}}_t$.

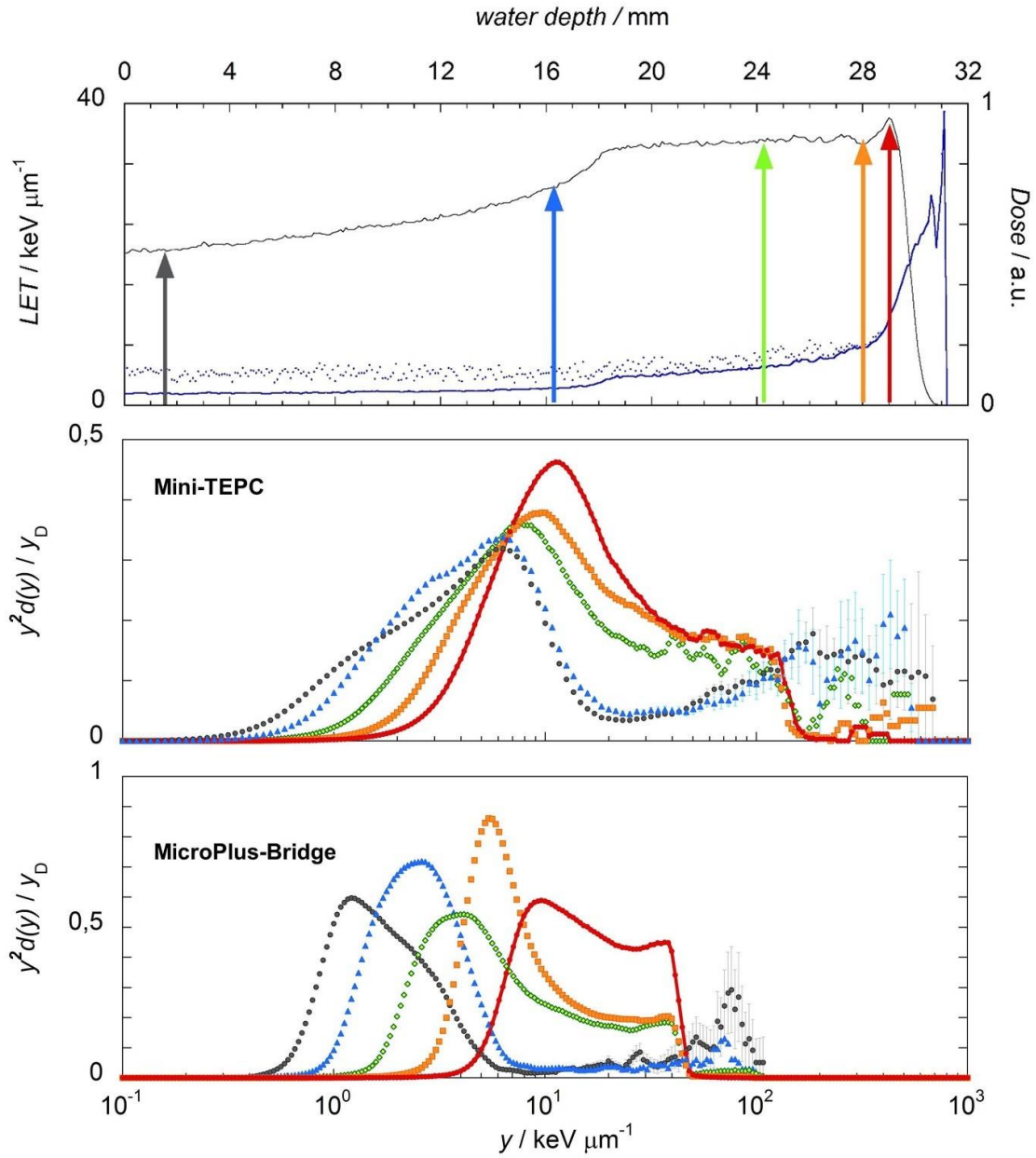


Figure 13. Microdosimetric $y^2 d(y)/\bar{y}_D$ spectra measured with the mini-TEPC at five depths, indicated by arrows in the depth dose profile. Equal area under the curves correspond to equal contribution to $\bar{y}_D$. Statistical uncertainties are shown for the entrance spectra only. The upper part shows the depth dose profile and the simulated primary (thin blue line) and total (blue dots) dose-averaged LET, $\overline{\mathrm{LET}}_d$, (see text for more details). The two bottom panels have the abscissa at the bottom; the upper panel has the abscissa on top.

The dose-mean lineal energy values derived from microdosimetric spectra measured with both detectors are shown in figure 15 as a function of depth. The total dose-averaged LET, which considers the secondary particles produced in nuclear interactions, is also plotted for comparison. In contrast to $\bar{y}_F$, values of $\bar{y}_D$ are less sensitive to the contribution from the lower-energy part of the spectrum and as a consequence, the agreement between the $\bar{y}_D$ measured with the mini-TEPC and the total $\overline{\mathrm{LET}}_d$ is very good. At the same time, $\bar{y}_D$ is strongly dependent on the variance of the lineal energy distribution, which explains why the 10 µm thick silicon device shows smaller $\bar{y}_D$ values up to the depth z = 29 mm, corresponding to the Bragg peak position. In the region of the Bragg peak the average energy deposit increases and the difference in the straggling plays a minor role, so that the $\bar{y}_D$ for the Bridge agrees both with the mini-TEPC and with the total $\overline{\mathrm{LET}}_d$ simulated data. Both the difference in the entrance region and the better agreement in the distal region are consistent with the results obtained in simulations performed in different SV sizes (Bolst *et al* 2020).

The $\overline{\mathrm{LET}}_d$ values obtained at entrance appear to be slightly larger than $\bar{y}_D$ measured with the mini-TEPC. Here, it is worth noticing that the calculated $\overline{\mathrm{LET}}_d$ considers the whole energy lost per unit depth, whereas the lineal energy considers only the energy deposited within the SV and misses the energy deposited outside

Table 1. Frequency and dose-mean lineal energy values derived from event size distributions measured with the mini-TEPC and the Bridge microdosimeter at different depth positions across the SOBP. The uncertainties on $\bar{y}_F$ and $\bar{y}_D$ were determined by error propagation following the uncertainty in the number of counts and that on the lineal energy calibration.

Water depth miniTEPC/mm	$\bar{y}_F$mini-TEPC/ keV/μm	$\bar{y}_D$ mini-TEPC/ keV/μm	Water depth Bridge/mm	$\bar{y}_F$ Bridge/ keV/μm	$\bar{y}_D$ Bridge/ keV/μm
1.4	0.82 ± 0.04	3.9 ± 0.2	1.4	1.19 ± 0.06	1.8 ± 0.1
3.1	0.97 ± 0.05	3.5 ± 0.2	2.8	1.22 ± 0.06	1.8 ± 0.1
4.9	1.01 ± 0.05	3.8 ± 0.2	4.2	1.25 ± 0.06	1.9 ± 0.1
6.7	1.05 ± 0.05	3.6 ± 0.2	5.7	1.28 ± 0.06	1.1 ± 0.1
8.4	1.08 ± 0.05	3.6 ± 0.2	7.1	1.32 ± 0.07	1.9 ± 0.1
10.2	1.13 ± 0.06	3.7 ± 0.2	8.5	1.31 ± 0.07	1.9 ± 0.1
11.9	1.19 ± 0.06	3.8 ± 0.2	9.9	1.40 ± 0.07	2.0 ± 0.1
14.4	1.18 ± 0.06	3.7 ± 0.2	11.3	1.42 ± 0.07	2.1 ± 0.1
15.5	1.35 ± 0.07	3.8 ± 0.2	12.7	1.47 ± 0.07	2.1 ± 0.1
16.2	1.28 ± 0.06	4.1 ± 0.2	14.1	1.54 ± 0.08	2.2 ± 0.1
16.9	1.43 ± 0.07	4.3 ± 0.2	15.5	1.64 ± 0.08	2.4 ± 0.1
17.6	1.53 ± 0.08	4.4 ± 0.2	16.2	1.73 ± 0.09	2.4 ± 0.1
18.3	1.50 ± 0.07	5.3 ± 0.3	16.9	1.79 ± 0.09	2.5 ± 0.1
19.0	1.73 ± 0.09	5.0 ± 0.3	17.6	1.86 ± 0.09	2.7 ± 0.1
19.7	1.59 ± 0.08	5.7 ± 0.3	18.4	2.0 ± 0.1	3.3 ± 0.2
20.5	1.79 ± 0.09	6.1 ± 0.3	19.1	2.3 ± 0.1	3.8 ± 0.2
20.8	1.89 ± 0.09	5.6 ± 0.3	19.8	2.4 ± 0.1	3.8 ± 0.2
22.0	1.86 ± 0.09	5.9 ± 0.3	20.5	2.4 ± 0.1	3.8 ± 0.2
22.5	2.1 ± 0.1	6.1 ± 0.3	21.2	2.5 ± 0.1	3.9 ± 0.2
23.0	2.0 ± 0.1	6.4 ± 0.3	21.9	2.5 ± 0.1	4.0 ± 0.2
24.3	2.4 ± 0.1	6.7 ± 0.3	22.6	2.6 ± 0.1	4.2 ± 0.2
25.8	2.7 ± 0.1	7.6 ± 0.4	22.9	2.7 ± 0.1	4.2 ± 0.2
26.5	2.9 ± 0.1	8.2 ± 0.4	23.3	2.8 ± 0.1	4.5 ± 0.2
27.2	3.2 ± 0.2	8.3 ± 0.4	23.7	2.9 ± 0.1	4.5 ± 0.2
27.8	3.8 ± 0.2	9.1 ± 0.5	24.4	3.0 ± 0.1	4.8 ± 0.2
28.0	3.8 ± 0.2	9.4 ± 0.5	25.1	3.2 ± 0.2	5.1 ± 0.3
28.6	4.2 ± 0.2	9.9 ± 0.5	25.8	3.5 ± 0.2	5.3 ± 0.3
29.1	4.8 ± 0.2	11.1 ± 0.6	26.5	3.8 ± 0.2	5.8 ± 0.3
29.3	5.7 ± 0.3	13.7 ± 0.7	27.2	4.4 ± 0.2	6.6 ± 0.3
29.7	7.2 ± 0.4	18.3 ± 0.9	27.9	5.0 ± 0.3	7.0 ± 0.4
30.0	8.8 ± 0.4	23 ± 1	28.2	5.7 ± 0.3	7.9 ± 0.4
30.4	12.5 ± 0.6	28 ± 1	28.6	7.0 ± 0.4	9.9 ± 0.5
30.8	15.7 ± 0.8	33 ± 2	28.9	8.8 ± 0.4	12.6 ± 0.6
–	–	–	29.3	10.7 ± 0.5	15.3 ± 0.8
–	–	–	29.7	12.4 ± 0.6	17.4 ± 0.9
–	–	–	30.0	13.2 ± 0.7	19 ± 1
–	–	–	30.4	14.5 ± 0.7	21 ± 1

SV by long-range secondary electrons. This effect, known as delta ray escape, is expected to be larger at the entrance, when the proton energy is higher and therefore the secondary electron range is longer. In addition, high LET target fragments stop inside the 10 μm thickness of the MicroPlus-Bridge microdosimeter, resulting in smaller lineal energy values, as it can be clearly observed in figure 13.

3.6. Comparison of assessed RBE values

The results for $RBE_{micro,scaled}(z)$ obtained from the two sets of microdosimetric spectra, one for each detector, are plotted in figure 16 as a function of depth. The RBE_{10} derived from cell survival curves for glioma U87 cells irradiated along the same proton beam line of Catana (Chaudhary *et al* 2014) are also shown in the figure. The $RBE_{micro,scaled}$ data show the same trend as the biological data: first they stay on a rather stable value of 1.1 up to the beginning of the SOBP plateau which is followed by a slight increase in the plateau region and finally a rapid increase in the distal region just before the Bragg peak and beyond it. These results are consistent with available radiobiological data from cell survival experiments (Britten *et al* 2013, Matsumoto *et al* 2014, Marshall *et al* 2016). A good agreement of the $RBE_{micro,scaled}$ of the two detectors is found within a 5% estimated uncertainty, and their prediction is consistent with radiobiological data when a 10% of uncertainty is assigned to biological data and 0.3 mm of uncertainty in depth is given to the position of the microdosimeters. The application of a biological weighting function is based on the assumption of a correlation between the single event $d(y)$ spectra and the RBE. Therefore the obtained result shown in figure 16 was not expected *a priori* given that (i) the spectra measured with the mini-TEPC and with the

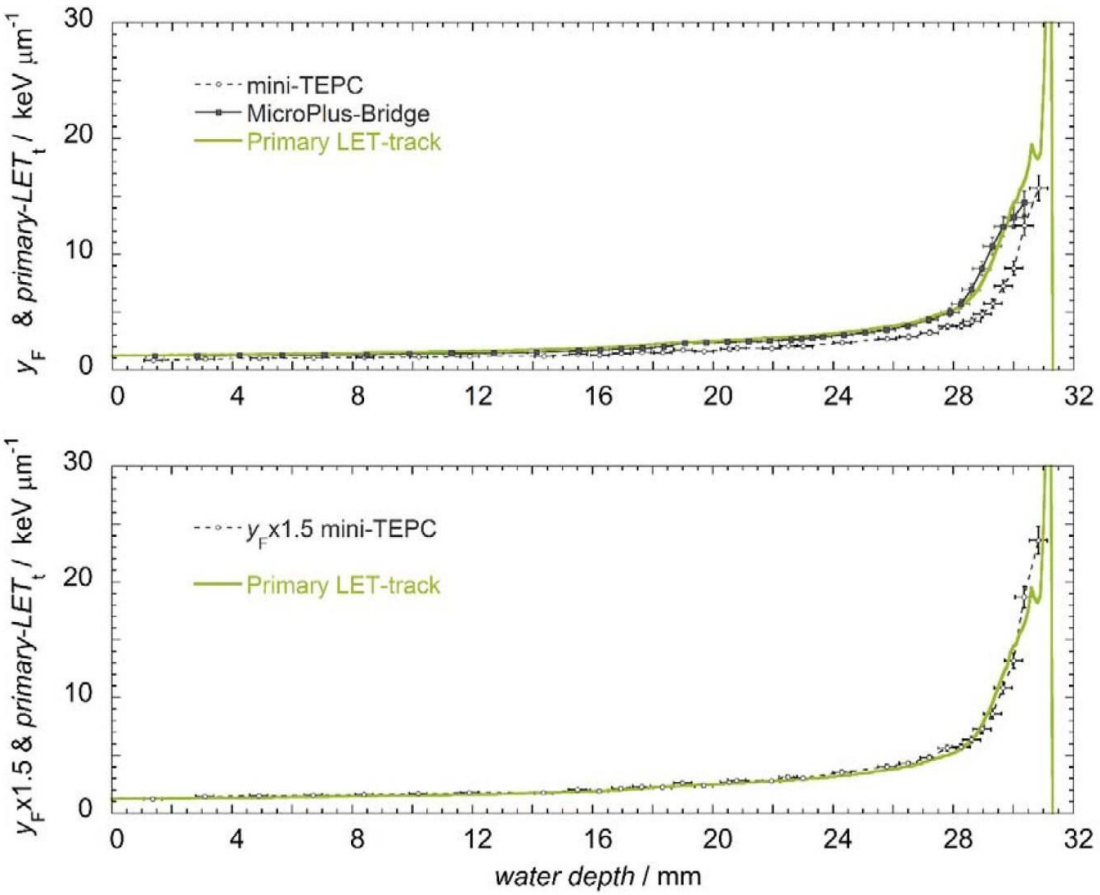


Figure 14. The mean lineal energy $\bar{y}_F$ derived from the microdosimetric spectra, compared to results of Geant4 Monte Carlo simulations for the track-averaged LET, $\overline{LET}_t$ (green line). Empty circles: mini-TEPC; filled squares: MicroPlus-Bridge detector. In the bottom panel, the $\bar{y}_F$ calculated from the mini-TEPC spectra was multiplied by a constant factor 1.5. Horizontal bars represent the 0.3 mm estimated uncertainty in the detectors' position. Vertical bars represent the uncertainties on $\bar{y}_F$ obtained by propagating the statistical uncertainties on the measured *f(y)* distributions and the uncertainty on the lineal energy calibration.

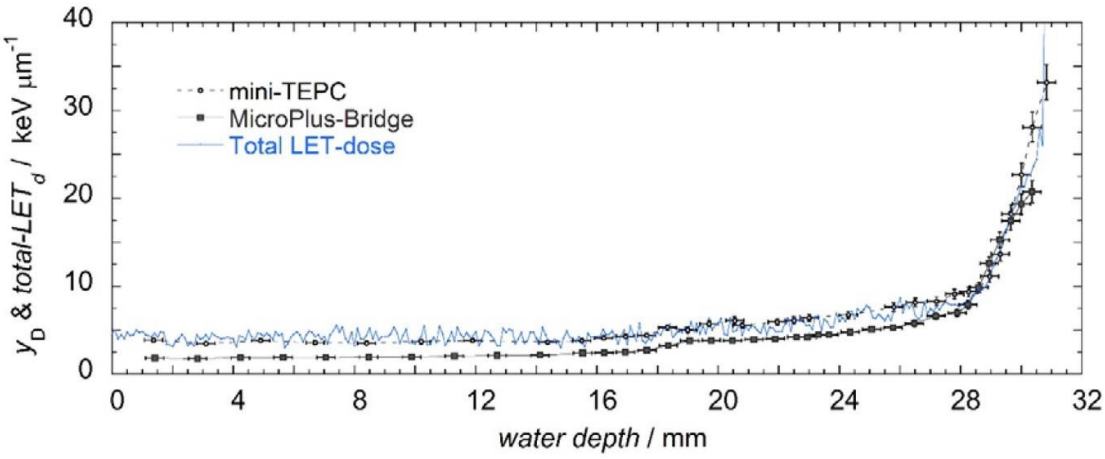


Figure 15. The dose-mean lineal energy $\bar{y}_D$ derived from the microdosimetric spectra, compared to results of Geant4 Monte Carlo simulations for the total dose-averaged LET (blue line). Empty circles: mini-TEPC; filled squares: Bridge microdosimeter. Horizontal bars represent the 0.3 mm estimated uncertainty in the detectors' position. Vertical bars represent the uncertainties on $\bar{y}_D$ obtained by propagating the statistical uncertainties on the measured d*(y)* distributions and the uncertainty on the lineal energy calibration.

Bridge detector differ significantly from each other and (ii) the Loncol's function r*(y)* is an empirical function that correlates a specific biological end-point with microdosimetric dose distributions measured at 2 µm tissue-equivalent size. The good agreement between the pairwise $RBE_{micro,scaled}$ values assessed with the

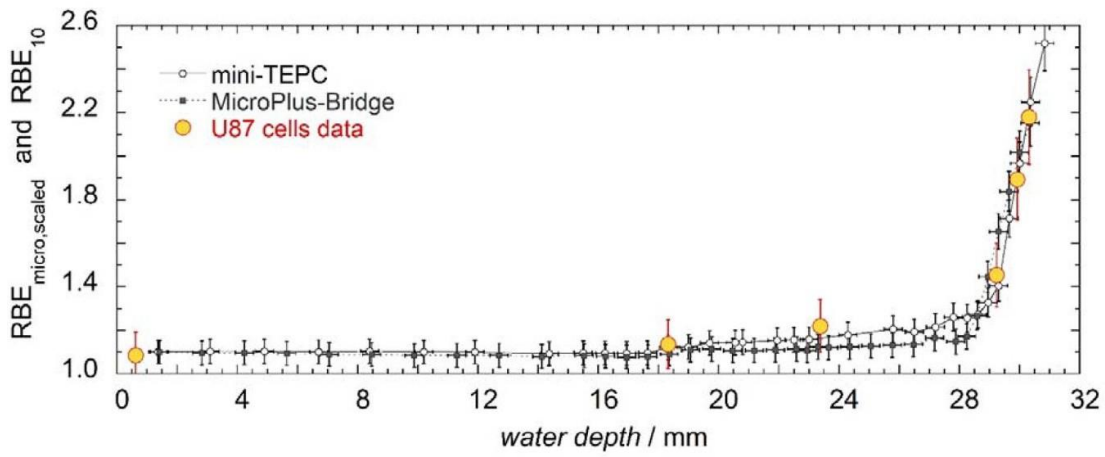


Figure 16. Water depth profile of the $RBE_{micro,scaled}$ values estimated from the microdosimetric spectra weighted with the Loncol's function according to equation (8) and scaled to the reference value of 1.1 in the first position. Empty circles: data corresponding to the mini-TEPC; filled squares: results from the Bridge microdosimeter. *RBE* data for 10% survival of U87 cells (Chaudhary *et al* 2014) irradiated on the same beam line are also shown in figure as coloured circles. Horizontal bars represent the 0.3 mm estimated uncertainty in the detectors' position. Vertical bars on $RBE_{micro,scaled}$ represent the uncertainties obtained by propagating the statistical uncertainties on the measured d*(y)* distributions and the uncertainty on the lineal energy calibration.

two different detectors suggests that the information contained in both the mini-TEPC and the MicroPlus-Bridge single event spectra d*(y)* is sufficient to assess the contribution of different radiation components to the overall biological effectiveness.

In order to study in greater detail the reasons for this final agreement on estimated RBE_{micro}, figure 17 shows the dose d*(y)* and the biological-weighted distributions r*(y)*d*(y)* at five positions across the SOBP, indicated by coloured arrows in the top panel of the figure. The middle panel shows the distributions obtained for the mini-TEPC, while the bottom panel shows results from the MicroPlus-Bridge detector. As usual, both distributions d*(y)* and r*(y)*d*(y)* were multiplied by *y*, so that equal area under each curve between two values of *y* correspond to equal relative contributions to the absorbed dose and to the RBE, respectively. Note that d*(y)* is the normalized dose distribution, while the integral of *r(y)*d*(y)* over the whole *y*-range, proportional to the area subtended by the *yr(y)*d*(y)* curve, is the RBE_{micro}, according to equation (8).

It can be observed that the *y*d*(y)* and the weighted *y*r*(y)*d*(y)* spectra are very similar to each other, when the main part of the *y*d*(y)* spectrum falls below $y = 10$ keV μm^{-1}. In this region of *y*-values the r*(y)* function is almost constant and equal to 1, therefore it has almost no effect when applied to the d*(y)* distribution. Consequently, the integral of the weighted distribution is equal to the integral of the d*(y)* distribution, which is equal to 1 by definition. Therefore, in the entrance channel, despite of the different shape of the d*(y)* distribution, the RBE_{micro} results equal to 1, or $RBE_{micro,scaled} = 1.1$ after the scaling. The contribution of rare high-*y* events, which is about 1% of the total dose and 45% of the total $\bar{y}_D$, though amplified by the *r(y)* weighting function, amounts to only 3% of the total RBE_{micro}. Therefore, at least for the 62 MeV modulated proton beam, the contribution of the target fragments seems to play a minor role, a result which is consistent with the observed radiobiological data.

When the spectral component above $y = 10$ keV μm^{-1} increases, in the region where the *r(y)* function also increases, the effect of the weighting function appears and become stronger as the *yd(y)* spectrum shifts to the right, in the region between 10 and 100 keV μm^{-1} where the *r(y)* shows its peak. By comparing the *yr(y)*d*(y)* curves in the mid and bottom panels, clearly the shape is rather different for the mini-TEPC and the Bridge detector.

Even if the shapes of the weighted distributions are different for the two detectors, the area under the curves, which represents the RBE_{micro} at the corresponding depth, is almost the same. This can be easily observed in figure 18, where the *yr(y)*d*(y)* spectra measured with the mini-TEPC (thick lines) and the MicroPlus-Bridge detector (thin lines) at four different positions (entrance, beginning of the plateau, Bragg Peak and fall-off) are directly compared. The reason for this is that, while the mini-TEPC spectra have both a low-*y* component and a high-*y* component that are not present in the Bridge spectra, the latter compensate their narrower distributions with a higher contribution in the intermediate-*y* interval, reaching higher values.

Finally, the impact of the variable RBE on the depth-dose profile is shown in figure 19. The physical dose D*(z)* is normalized to the centre of the SOBP. The biologically effective dose (BED) is calculated as D*(z)*x1.1, as in the clinical prescription, or alternatively as the scaled - $RBE_{micro}(z)$ at each depth multiplied by the physical dose D*(z)* at that depth. The scaled - $RBE_{micro}(z)$ are calculated from the mini-TEPC and the

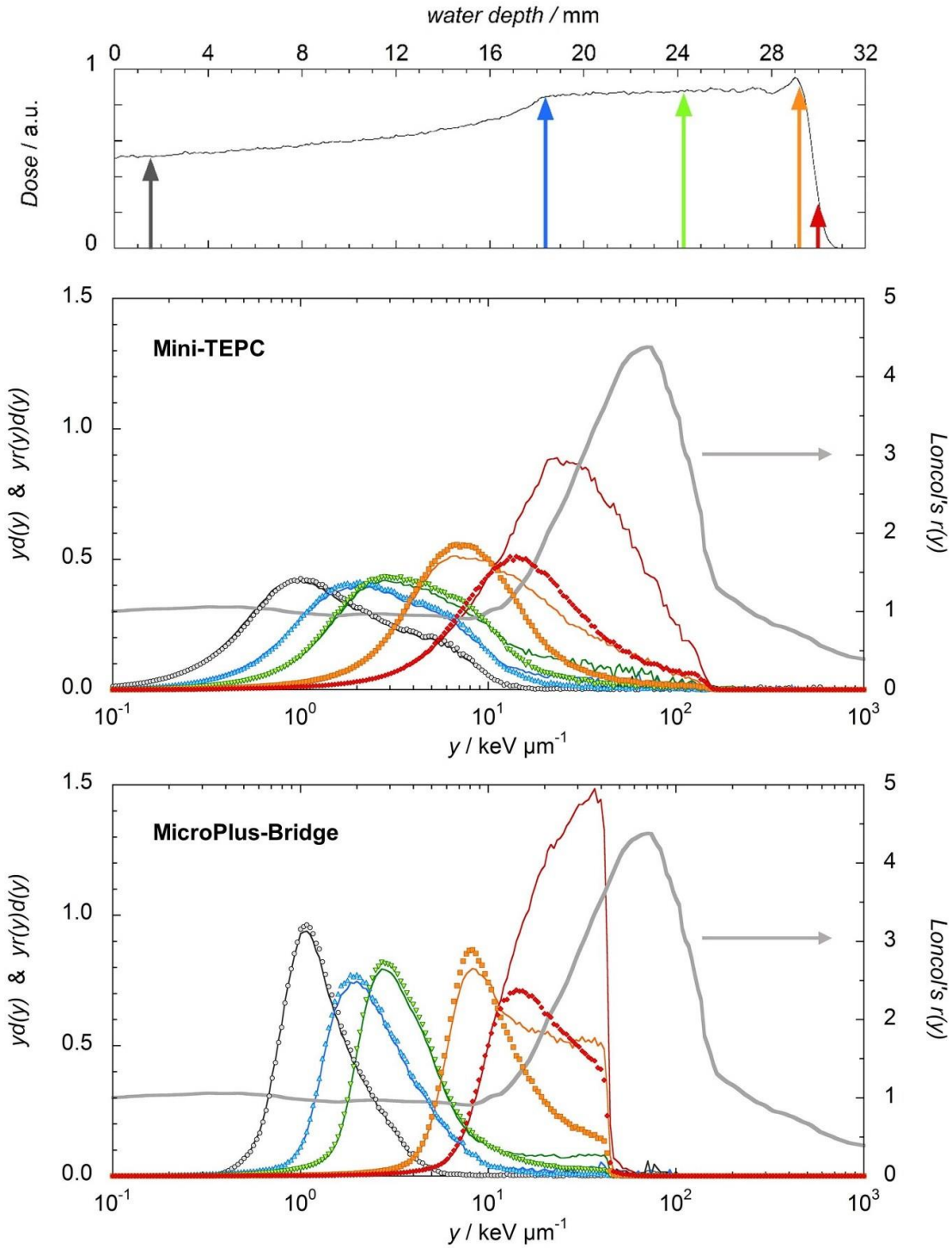


Figure 17. *Yd(y)* distributions (symbols) and biologically weighted *yr(y)*d*(y)* microdosimetric spectra (lines) for the mini-TEPC (mid-panel) and the MicroPlus-Bridge microdosimeter (bottom panel) at five relevant positions along the SOBP, indicated by arrows in the depth-dose profile shown in the top-panel. The Loncol's biological weighting function used is also shown in the plots as a thick grey line.

MicroPlus-Bridge dose distributions d*(y)*, according to equations (8) and (9). In both cases the biological effective doses are slightly higher than the clinical dose (BED 1.1) at the centre of the SOBP, and they significantly increase at a depth equal to $z = 29$ mm, in correspondence of the Bragg peak. Here, the mini-TEPC and the MicroPlus-Bridge system give effective doses that are about 30% and 60% higher than in the mid-SOBP, respectively. The larger value for the MicroPlus-Bridge is possibly due to the 0.3 mm uncertainty in position of both microdosimeters, the significance of which is amplified at the distal edge of the SOBP. The increase of RBE_{micro} in the distal and fall-off regions results in an extension of the bio-effective range of the proton beam in patients, which amounts to about 0.5 mm according to figure 19. Furthermore,

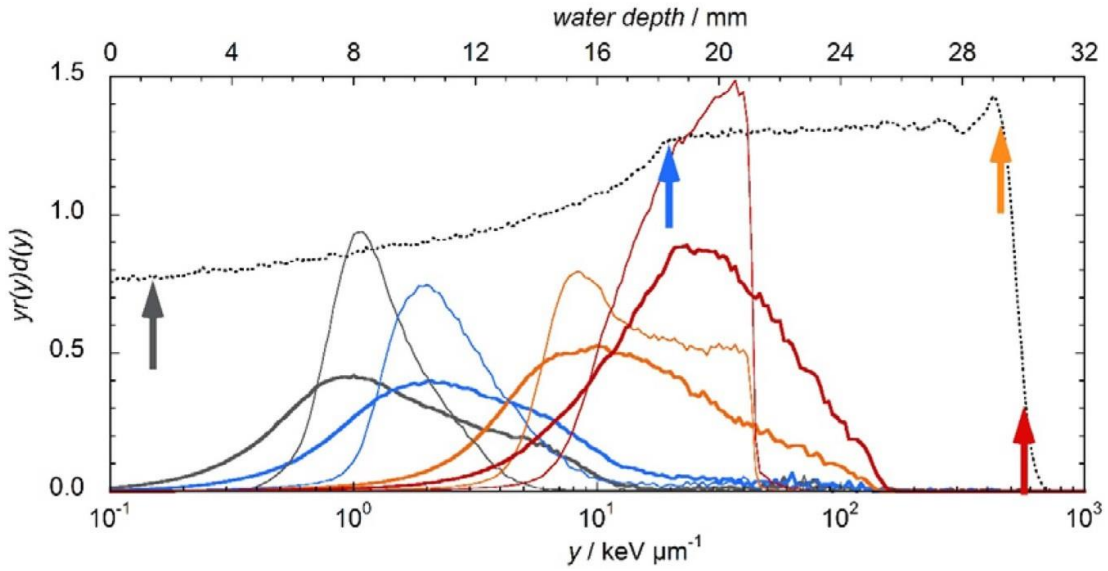


Figure 18. The biologically-weighted dose distributions *yr(y)*d*(y)* for the mini-TEPC (thick lines) and the MicroPlus-Bridge detector (thin lines) at four relevant positions along the SOBP, indicated by arrows in the depth-dose profile. Dose is in arbitrary units in this plot. The area under each curve represents the RBE_{micro} evaluated at the corresponding depth.

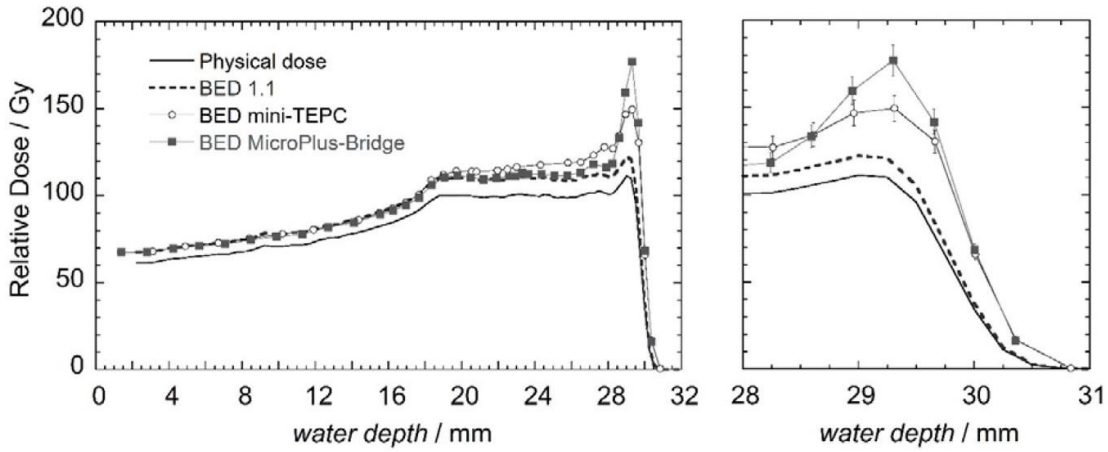


Figure 19. The physical dose (solid line) and the biological doses evaluated with the mini-TEPC and with the Bridge microdosimeter as a function of depth.

it is known that the RBE increases with decreasing dose i.e. with increasing survival fraction; for instance, Chaudhary *et al* found for the U87 cells that the RBE in the distal edge is 2.2 at 10% survival and increases to 3.5 at 50% survival (Chaudhary *et al* 2014). Therefore, the biologically effective dose in the exit region behind the tumour may be even higher than that estimated in this work. The consequent range extension should be considered during the treatment planning to avoid damage of organs at risk.

4. Conclusions

Microdosimetric spectra were measured across the 62 MeV therapeutic modulated proton beam of CATANA with a mini-TEPC, simulating a 0.85 µm water site size, and a 10 µm thick SOI MicroPlus-Bridge microdosimeter at 33 and 37 different positions, respectively. The distributions measured with the mini-TEPC are always broader than the corresponding ones measured by the Bridge microdosimeter, mainly because the energy straggling is larger in the smaller 0.85 µm volume, but also because of the additional contributions to the variance of the mini-TEPC spectra due to several factors, as for instance the chord length variability and the gas avalanche stochastics. The secondary electrons generated in the cavity walls and injected into the SV also contribute to the broadening of the mini-TEPC spectrum at the entrance, because the maximum energy deposited by electrons in 0.85 µm is about 7 keV, higher than that deposited by

60 MeV protons in the same site, which is about 1 keV. For the 10 μm site of the Bridge the size of electrons and protons events is similar, thus producing a single narrower peak.

The difference between the TEPC and SOI spectra increases towards the Bragg peak, because slow protons with energy smaller than 715 keV stop inside the 10 μm thickness of the silicon device, resulting in smaller lineal energy values, which is most relevant at the end of the proton range. Despite the markedly different microdosimetric spectra, when the Loncol's weighting function is applied to the dose distributions both detectors lead to an assessment of the RBE_{10} that is in good agreement with radiobiological data for glioma U87 cells obtained in the same beam line, if the 10% biological uncertainty is taken into account. The good agreement of the RBE_{micro} values is due to a compensation of several spectral contributions resulting in a similar integral value. Therefore, both the mini-TEPC and the silicon Bridge microdosimeters can be used to model the RBE of 62 MeV proton irradiation experiments across the whole SOBP. Further studies are ongoing to verify whether similar conclusions can also be drawn for higher energy therapeutic proton beams used to treat deep tumours.

Acknowledgments

This work has been supported by the Italian Institute for Nuclear Physics (INFN), within the framework of the research project 'Neptune'.

References

Allison J *et al* 2016 Recent developments in GEANT4 *Nucl. Instrum. Methods* A **835** 186–225

Anderson S *et al* 2017 Microdosimetric measurements of a clinical proton beam with micrometer-sized solid-state detector *Med. Phys.* **44** 6029–37

Berger M J 1993 Penetration of proton beams through water I. depth-dose distribution, spectra and LET distribution *NISTIR Publication* 5226 (Gaithersburg, MD: National Institute of Standards and Technology) (https://nvlpubs.nist.gov/nistpubs/Legacy/IR/nistir5226.pdf)

Bertolet A, Cort´es-Giraldo M A and Carabe-Fernandez A 2020 On the concepts of dose-mean lineal energy, unrestricted and restricted dose-averaged LET in proton therapy *Phys. Med. Biol.* **65** 075011

Bianchi A *et al* 2020 Microdosimetry with a sealed mini-TEPC and a silicon telescope at a clinical proton SOBP of CATANA *Radiat. Phys. Chem.* **171** 108730

Bolst D, Guatelli S, Tran L T, Chartier L, Lerch M L F, Matsufuji N and Rosenfeld A B 2017 Correction factors to convert microdosimetry measurements in silicon to tissue in 12C ion therapy *Phys. Med. Biol.* **62** 2055–69

Bolst D, Guatelli S, Tran L T and Rosenfeld A B 2020 The impact of sensitive volume thickness for silicon on insulator microdosimeters in hadron therapy *Phys. Med. Biol.* **65** 035004

Britten R A, Nazaryan V, Davis L K, Klein S B, Nichiporov D, Mendonca M S, Wolanski M, Nie X, George J and Keppel C 2013 Variations in the RBE for cell killing along the depth dose profile of a modulated proton therapy beam *Radiat. Res.* **179** 21–28

Chaudhary P *et al* 2014 Relative biological effectiveness variation along monoenergetic and modulated Bragg peaks of a 62-MeV therapeutic proton beam: a preclinical assessment *Int. J. Radiat. Oncol. Biol. Phys.* **90** 27–35 (PubMed: 24986743)

Cirrone G A P *et al* 2017 Clinical and research activities at the CATANA facility of INFN-LNS: from the conventional hadrontherapy to the laser-driven approach *Front. Oncol.* **7** 223

Cirrone G A P, Cuttone G, Di Rosa F, Raffaele L, Russo G, Guatelli S and Pia M G 2006 The geant4 toolkit capability in the hadron therapy field: simulation of a transport beam line *Nucl. Phys.* B **150** 54–57

Colautti P, Bianchi A, Selva A, Bortot D, Mazzucconi D, Pola A, Agosteo S, Petringa G, Cirrone G A P and Conte V 2020 Therapeutic proton beams: *LET*, RBE and microdosimetric spectra with gas and silicon detectors *Radiat. Meas.* **136** 106386

Conte V, Bianchi A, Selva A, Petringa G, Cirrone G A P, Parisi A, Vanhavere F and Colautti P 2019 Microdosimetry at the CATANA 62 MeV proton beam with a sealed miniaturized TEPC *Phys. Med.* **62** 114–22

Conte V, Moro D, Grosswendt B and Colautti P 2013 Linear energy calibration of mini tissue equivalent gas-proportional counters (TEPC) *Multidisciplinary Applications of Nuclear Physics with Ion Beams (ION BEAMS '12) – AIP Conf. Proc.* **1530** 171–8

Cort´es-Giraldo M A and Carabe A 2015 A critical study of different Monte Carlo scoring methods of dose average linear-energy-transfer maps calculated in voxelized geometries irradiated with clinical proton beams *Phys. Med. Biol.* **60** 2645–69

De Nardo L *et al* 2004 Microdosimetric assessment of Nice therapeutic proton beam biological quality *Phys. Med.* **20** 71–77

Debrot E *et al* 2018 SOI microdosimetry and modified MKM for evaluation of relative biological effectiveness for a passive proton therapy radiation field *Phys. Med. Biol.* **63** 235007

Deng W, Ding X, Younkin J E, Shen J, Bues M, Schild S E, Patel S H and Liu L W 2020 3D analytical linear energy transfer calculation algorithm based on precalculated data from Monte Carlo simulations *Med. Phys.* **47** 745–52

Durante M 2019 Proton beam therapy in Europe: more centres need more research *Br. J. Cancer* **120** 777–8

Giantsoudi D *et al* 2013 Linear energy transfer-guided optimization in intensity modulated proton therapy: feasibility study and clinical potential *Int. J. Radiat. Oncol. Biol. Phys.* **87** 216–22

Granville D A and Sawakuchi G O 2015 Comparison of linear energy transfer scoring techniques in Monte Carlo simulations of proton beams *Phys. Med. Biol.* **60** N283–91

Grassberger C and Paganetti H 2011 Elevated LET components in clinical proton beams *Phys. Med. Biol.* **56** 6677–91
Guan F *et al* 2015 Spatial mapping of the biologic effectiveness of scanned particle beams: towards biologically optimized particle therapy *Sci. Rep.* **5** 9850
Guan F *et al* 2018 RBE model-based biological dose optimization for proton radiobiology studies *Int. J. Part. Ther.* **5** 160–71
Guatelli S, Reinhard M I, Mascialino B, Prokopovich D A, Dzurak A S, Zaider M and Rosenfeld A B 2008 Tissue equivalence correction in silicon microdosimetry for protons characteristic of the LEO space environment *IEEE Trans. Nucl. Sci.* **55** 6
Hirayama S *et al* 2018 An analytical dose-averaged LET calculation algorithm considering the off-axis LET enhancement by secondary protons for spot-scanning proton therapy *Med. Phys.* **45** 3404–16
ICRU 1983 ICRU Report 36: Microdosimetry (os-19 Issue 1, December 1983)
ICRU 1998 Fundamental quantities and units for ionizing radiation Report 60 International Commission on Radiation Units and Measurements (Bethesda, MD)
ICRU (International Commission on Radiation Units and Measurements) and IAEA (International Atomic Energy Agency) 2007 Prescribing, recording and reporting proton-beam therapy *ICRU Report 78, jointly with the IAEA, JICRU* vol 7 (Oxford: Oxford University Press)
Jones B, Mcmahon S J and Prise K M 2018 The radiobiology of proton therapy: challenges and opportunities around relative biological effectiveness *Clin. Oncol.* **30** 285–92
Kellerer A M 1985 Fundamentals of microdosimetry *Dosimetry of Ionizing Radiation* vol 1 eds K R Kase, B E Bjamgard and F H Attix (New York: Academic) pp 77–162 (https://core.ac.uk/download/pdf/12169582.pdf)
Kobetich E J and Katz R 1969 Electron energy dissipation *Nucl. Instr. And Meth.* **71** 226–30
Loncol T, Cosgrove V, Denis J M, Gueulette J, Mazal A, Menzel H G, Pihet P and Sabattier R 1994 Radiobiological effectiveness of radiation beams with broad LET spectra: microdosimetric analysis using biological weighting functions *Radiat. Prot. Dosim.* **52** 347–52
Ma D *et al* 2020 Exploring the advantages of intensity-modulated proton therapy: experimental validation of biological effects using two different beam intensity-modulation patterns *Sci. Rep.* **10** 3199
Marshall T I, Chaudhary P, Michaelidesov´a A, Vachelov´a J, Davídkov´a M, Vondr´aˇcek V, Schettino G and Prise K M 2016 Investigating the implications of a variable rbe on proton dose fractionation across a clinical pencil beam scanned spread-out Bragg peak *Int. J. Radiat. Oncol. Biol. Phys.* **95** 70–77
Marsolat F, De Marzi L, Pouzoulet F and Mazal A 2016 Analytical linear energy transfer model including secondary particles: calculations along the central axis of the proton pencil beam *Phys. Med. Biol.* **61** 740–57
Matsumoto Y, Matsuura T, Wada M, Egashira Y, Nishio T and Furusawa Y 2014 Enhanced radiobiological effects at the distal end of a clinical proton beam: in vitro study *J. Radiat. Res.* **55** 816–22
Mazzucconi D, Bortot D, Pola A, Fazzi A, Colautti P, Conte V, Petringa G, Cirrone G A P and Agosteo S 2019 Nano-microdosimetric investigation at the therapeutic proton irradiation line of CATANA *Radiat. Meas.* **123** 26–33
McNamara A L, Schuemann J and Paganetti H 2015 A phenomenological relative biological effectiveness (RBE) model for proton therapy based on all published in vitro cell survival data *Phys. Med. Biol.* **60** 8399–416
Mohan R, Peeler C R, Guan F, Bronk L, Cao W and Grosshans D R 2017 Radiobiological issues in proton therapy *Acta Oncol.* **56** 1367–73
Paganetti H *et al* 2002 Nuclear interactions in proton therapy: dose and relative biological effect distributions originating from primary and secondary particles *Phys. Med. Biol.* **47** 747
Paganetti H 2014 Relative biological effectiveness (RBE) values for proton beam therapy. Variations as a function of biological endpoint, dose, and linear energy transfer *Phys. Med. Biol.* **59** R419–72
Peeler C R, Mirkovic D, Titt U, Blanchard P, Gunther J R, Mahajan A, Mohan R and Grosshans D R 2016 Clinical evidence of variable proton biological effectiveness in pediatric patients treated for ependymoma *Radiother. Oncol.* **121** 395–401
Petringa G *et al* 2017 Development and analysis of the track-, dose-LET and RBE calculations with a therapeutical proton and ion beams using Geant4 Monte Carlo code *Phys. Med.* **42** 9
Petringa G *et al* 2020 Monte Carlo implementation of new algorithms for the averaged-dose and -track linear energy transfer evaluation in 62 MeV clinical proton beams *Phys. Med. Biol.* in press. (https://doi.org/10.1088/1361-6560/abaeb9)
Polf J C, Mackin D, Lee E, Avery S and Beddar S 2014 Detecting prompt gamma emission during proton therapy: the effects of detector size and distance from the patient *Phys. Med. Biol.* **59** 2325–40
PSTAR 2020 Stopping Power and range tables for protons (available at: https://physics.nist.gov/PhysRefData/Star/Text/PSTAR.html)
Rollet S, Colautti P, Grosswendt B, Herault J, Wind M, Gargioni E, Beck P, Latocha M and Moro D 2011 Microdosimetric assessment of the radiation quality of a therapeutic proton beam: comparison between numerical simulation and experimental measurements *Radiat. Prot. Dosim.* **143** 445–9
Rollet S, Colautti P, Grosswendt B, Moro D, Gargioni E, Conte V and Denardo L 2010 Monte Carlo simulation of mini TEPC microdosimetric spectra: influence of low energy electrons *Radiat. Meas.* **45** 1330–3
Rosenfeld A B 2016 Novel detectors for silicon based microdosimetry, their concepts and applications NIM A *Advanced in Detectors and Application for Medicine* eds F Sauli, A Del Guerra, A Olivo and P Thirolf **809** 156–70
Sanchez-Parcerisa D, Cort´es-Giraldo M A, Dolney D, Kondrla M, Fager M and Carabe A 2016 Analytical calculation of proton linear energy transfer in voxelized geometries including secondary protons *Phys. Med. Biol.* **61** 1705–21
Seltzer S M 1993 An assessment of the role of charged secondaries from nonelastic nuclear interactions by therapy protons beams in water *NISTIR Publication* 5221 (Gaithersburg, MD: National Institute of Standards and Technology) (https://nvlpubs.nist.gov/nistpubs/Legacy/IR/nistir5221.pdf)
Sørensen B S, Bassler N, Nielsen S, McNamarahorsman M R, Grzanka L, Spejlborg H, Swakon´ J, Olko P and Overgaard J 2017 Relative biological effectiveness (RBE) and distal edge effects of proton radiation on early damage in vivo *Acta Oncol.* **56** 1387–91
Tommasino F and Durante M 2015 Proton radiobiology *Cancers* **7** 353–81
Tran L T *et al* 2015 3D-Mesa 'Bridge' silicon microdosimeter: charge collection study and application to RBE studies in 12C radiation therapy *IEEE Trans. Nucl. Sci.* **62** 504–11
Wagenaar D *et al* 2020 Validation of linear energy transfer computed in a Monte Carlo dose engine of a commercial treatment planning system *Phys. Med. Biol.* **65** 025006
Waker A J 1985 Experimental uncertainties in microdosimetric measurements and an examination of the performance of three commercially produced proportional counters *Nucl. Instrum. Methods Phys. Res.* A **234** pp 354–360
Weber K H 1964 Eine einfache reichweite-energie-beziehung fur elektronen im energiebereich von 3 keV bis 3 MeV *Nucl. Instr. and Meth.* **25** 261–4
Wilkens J and Oelfke U 2002 Analytical linear energy transfer calculations for proton therapy *Med. Phys.* **30** 806
Ziegler J F, Ziegler M D and Biersack J P 2010 SRIM the stopping and range of ions in matter *Nucl. Instrum. Methods* B **268** 1818–23